Soil-reinforcement interaction: Stress regime evolution in geosynthetic-reinforced soils

Amr M. Morsy [a,b,*], Jorge G. Zornberg [c]

[a] School of Architecture, Building and Civil Engineering, Loughborough University, Loughborough, LE11 3TU, United Kingdom
[b] Department of Civil Engineering, Cairo University, Giza, 12613, Egypt
[c] Department of Civil, Architectural, and Environmental Engineering, The University of Texas at Austin, Texas, 78712, United States

ARTICLE INFO

ABSTRACT

Understanding the stress regime that develops in the vicinity of reinforcements in reinforced soil masses may prove crucial to understanding, quantifying, and modeling the behavior of a reinforced soil structures. This paper presents analyses conducted to describe the evolution of stress and strain fields in a reinforced soil unit cell, which occur as shear stresses are induced at the soil-reinforcement interface. The analyses were carried out based on thorough measurements obtained when conducting soil-reinforcement interaction tests using a new large-scale device developed to specifically assess geosynthetic-reinforced soil behavior considering varying reinforcement vertical spacings. These experiments involved testing a geosynthetic-reinforced mass with three reinforcement layers: an actively tensioned layer and two passively tensioned neighboring layers. Shear stresses from the actively tensioned reinforcement were conveyed to the passively tensioned reinforcement layers through the intermediate soil medium. The experimental measurements considered in the analyses presented herein include tensile strains developed in the reinforcement layers and the displacement field of soil particles adjacent to the reinforcement layers. The analyses provided insights into the lateral confining effect of geosynthetic reinforcements on reinforced soils. It was concluded that the change in the lateral earth pressure increases with increasing reinforcement tensile strain and reinforcement vertical spacing, and it decreases with increasing vertical stress.

1. Introduction

The use of soil reinforcement has been widely recognized as an alternative to conventional design of many geotechnical systems. It involves placement of reinforcement inclusions, such as planar geosynthetics between compacted soil layers to provide tensile strength to the soil mass. These layers intercept potential shear failure surfaces that tend to form within a soil structure, developing tensile forces that provide stability to an otherwise unstable soil mass (e.g., Palmeira, 2009). Conventional design of such reinforced soil systems focuses on determination of the overall tensile capacity of the reinforcing inclusions, although designs are often insensitive to the distribution of the inclusions within the soil structure (i.e., reinforcement vertical spacing). Some studies have pointed toward the relevance of interactions that may develop among reinforcement layers, rendering a behavior that has often been described as that of a composite material. Such behavior was reported to have occurred in systems in which the reinforcement spacing is comparatively small (e.g., Leshchinsky et al. 1994; Leshchinsky and Vulova, 2001; Wu et al. 2013; Nicks et al. 2013; Morsy, 2017; Morsy et al. 2017a, 2017b, 2019a, 2020; Wu, 2019; Xu et al. 2019, 2020).

While extensive research has been conducted to characterize the interaction and associated loading mechanisms that occur at the actual soil-reinforcement interface (e.g., Juran et al. 1988; Ochiai et al. 1996; Palmeria, 2009; Roodi et al. 2018; Djeffal and Belkacemi, 2020), very limited research has been conducted to characterize the load transfer occurring beyond such interface. Recent studies showed that the load transfer beyond the actual interface controls the interaction between neighboring reinforcement layers, which increases with increasing transferred load (Morsy, 2017; Zornberg et al. 2018, 2019; Morsy et al., 2019a, 2020). Overall, these studies point to an increasing load transfer between neighboring reinforcement layers with decreasing reinforcement vertical spacing. The interaction between reinforcements and the surrounding soil, as well as interaction among reinforcement layers, plays a relevant role in the overall mechanical response of a reinforced

---

* Corresponding author.
  E-mail address: a.morsy@lboro.ac.uk (A.M. Morsy).

soil mass when the reinforcement vertical spacing is comparatively small.

A limited number of studies were conducted to capture the deformation of a reinforced soil mass away from the soil-reinforcement interface that result from soil-reinforcement interaction (Kharchafi and Dysli, 1993; Alagiyawanna et al. 2001; Morsy et al. 2018, 2019b; Lashkari and Jamali, 2020). Kharchafi and Dysli (1993) studied the anchorage of geotextile reinforcements in embankments and retaining walls. In their study, several pullout tests were conducted with nonwoven geotextiles embedded in dry sand and damp silt fills. X-ray radiography was used to visualize and quantify movements within the soil and reinforcement during testing. The researchers reported that the thickness of the soil shear zone increased with increasing reinforcement stiffness. They observed that soil displacements were greater when using a silt (fine-grained soil) than when considering a sand (coarse-grained soil). Additionally, the thickness of the shear zone was observed to decrease with increasing normal stresses in tests conducted using a sand backfill while, in tests conducting using a silt backfill, the thickness of the shear zone appeared to be independent of the applied normal stresses. Similarly, Alagiyawanna et al. (2001) used X-ray radiography in pullout tests conducted on highly extensible geogrid reinforcements with different ratios of longitudinal to transverse member counts embedded in sand fill. They observed that the mobilization of soil-reinforcement bond stress (sum of mobilized interface shear and bearing stresses) depended on reinforcement strains, where the bond stress was found to increase linearly up to reinforcement strains of 3–4%, followed by a bond stress decrease up to reinforcement rupture. This decrease was reported to occur when slippage occurred at the soil-reinforcement interface. Alagiyawanna et al. (2001) concluded that the influence zones of geogrid longitudinal members become isolated once the grid apertures become sufficiently wide (i.e., the spacing between longitudinal members). They attributed this to a decrease in bending stiffness of the transverse members, thus allowing their deformation during pullout. Furthermore, Alagiyawanna et al. (2001) concluded that the uniformity of the soil-reinforcement bond stress distribution increases with increasing of the length of grid apertures (i.e., the spacing between transverse members). Overall, the contribution of geogrid longitudinal members to pullout resistance was determined to be more significant than that of transverse members at initial load levels (during geogrid deformation compatible with that of the soil, prior to slippage). This was possibly due to a delayed full mobilization of transverse members. Peng and Zornberg (2017) used a small-scale pullout testing device equipped with laser-aided imaging to conduct pullout tests on geogrid reinforcements embedded in transparent sand surrogate (fused quartz) saturated with mineral oil mixture of the same refractive index as the sand surrogate. They measured soil displacements and geogrid deformations under pullout loading condition. The measured field displacements provided insights into the load transfer mechanisms at soil-reinforcement interfaces.

Several research studies were conducted to evaluate the soil deformation in the vicinity of soil-structure interfaces (e.g., Abramento and Whittle, 1995; Hu and Pu, 2004; Edil et al. 2005; Ebrahimian et al. 2012). Hu and Pu (2004) and Edil et al. (2005) used digital imaging techniques with direct shear tests to study the mechanical characteristics of soil-structure interfaces involving sands. Digital imaging was utilized to visualize and measure the movement of soil particles at the interface. Hu and Pu (2004) reported that two different failure modes occurred during interface shear failure: elastic perfect-plastic failure mode occurred for smooth interfaces; and strain localization in conjunction with strong strain-softening and bulk dilatancy failure mode occurred for rough interfaces. Edil et al. (2005) investigated the effects of grain size and structural surface roughness on soil-structure interface shear transfer behavior. They concluded that the soil-structure interface strength increases with increasing interface roughness. In addition, the zone of shear transfer was observed to increase with increasing interface roughness. Edil et al. (2005) also reported that soils with large particles

exhibit a comparatively smaller zone of shear transfer than soils with small particles for a given interface roughness. Additionally, soils with angular particles were reported to exhibit a larger zone of shear transfer and interface strength than soils with round particles. Morsy et al. (2018) conducted an experimental study to evaluate the shear band that forms at soil-geotextile interfaces using pullout and direct shear interface shear loading mechanisms. They concluded that the influence zone that the soil-reinforcement interface has on the adjacent soil is smaller in pullout than in direct shear for the same relative shear displacement between soil and reinforcement. It was also concluded that the influence zone of the soil-reinforcement interface has on the adjacent soil increases with increasing normal stress.

Ebrahimian et al. (2012) studied the shear localization along soil-structure interfaces of granular soils and structural surfaces at large shearing displacements. The researchers conducted finite element simulations adopting the Cosserat continuum approach in an elasto-plasticity framework. Specifically, they investigated the effects of different kinematic boundary conditions along the soil-structure interface on the evolution and thickness of the shear band. They concluded that the normal and shear stress distributions within a soil layer at increasing normal distances from a moving boundary depend significantly on the magnitude of horizontal displacement of the boundary. The non-uniformity of stress distributions was observed to increase across the thickness of the soil layer with increasing the bounding structure displacement. Moreover, Ebrahimian et al. (2012) reported that shear localization initiates as soon as shearing begins, and that he location and thickness of the shear band depend significantly on the soil initial void ratio and grain size distribution, although it was comparatively independent of the normal stress. It was observed that the thickness of localized shear changed with the magnitude of shear deformations, and that the shear band thickness increased with increasing void ratio, normal stress, grain size and particle rotation resistance along the interface.

The study presented in this paper includes the data analyses and development of a proposed model aimed at describing the evolution of stress and strain fields around a reinforcement inclusion in a reinforced soil system during shear stress generation at the soil-reinforcement interface. The model was calibrated using experimental results generated using a new experimental approach developed by Morsy (2017) and Morsy et al. (2019b). Finally, relevant insights into the effect of reinforcement vertical spacing on the behavior of reinforced soil structures are presented.

2. Conceptual model to represent the interaction among reinforcements in a group

A system representative of a group of reinforcements in a reinforced soil mass can be thought of one consisting of three reinforcement layers. Typically, the reinforcements in reinforced soil systems are subjected to axial tensile loads resulting from the lateral spreading of the surrounding soil mass. The load transfer from an active reinforcement to the neighboring passive reinforcements was evaluated in this research to assess the interaction among neighboring reinforcement layers. The interaction from one active reinforcement in a three-reinforcement system can then be applied to a larger group of active reinforcements by superposition. Evaluation of this concept benefits from the availability of experimental data reported by Morsy (2017) and Morsy et al. (2019a, 2020) that could quantify the zone of influence of an active reinforcement on neighboring reinforcements. The soil deformation was obtained experimentally by Morsy (2017), which includes both elastic and plastic deformation of the reinforced soil. The analyses conducted in this study focus on deformations that correspond to operational loads in reinforced soil structures. A similar modeling approach was adopted by Rotta Loria and Laloui (2016) to study the interaction between piles in a pile group system. The load transfer among reinforcement layers takes place through the intermediate medium (i.e., sandwiched soil layer).

Force chains develop among soil particles as shear stresses are generated at the interfaces between soil and the an individual actively tensioned reinforcement. These force chains spread within an influence zone where energy dissipates. In conditions involving multiple active reinforcements, energy is transferred to each soil layer from the interfaces with the two bounding reinforcement layers. Fig. 1 shows a schematic representation of the superposition concept adopted in this study, which is consistent with the layout of the experimental device described by Morsy (2017). This schematic representation was developed based on the observations of Leshchinsky et al. (1994) and Morsy et al. (2017).

3. Summary of experimental information

A new experimental device was designed and implemented by Morsy (2017) at the University of Texas at Austin to evaluate soil-reinforcement composite behavior and quantify the thickness of the zone where shear stresses propagate into the soil adjacent to the interface with a reinforcement where shear stresses are imposed. The device was used to conduct soil-geosynthetic interaction tests with various geosynthetic and soil materials under varied testing conditions. The results of these tests, presented in Morsy (2017) and Morsy et al. (2019a, 2020), are used to calibrate the model developed in the present study. This section provides a descriptive summary of the soil-geosynthetic interaction device, its instrumentation, and the scope of the previously reported experimental tests with emphasis on the information relevant to the development of the subsequently presented model.

3.1. Soil-geosynthetic interaction device

The device consisted of a steel box designed to accommodate soil specimens up to 1200 mm in depth, 750 mm in width and 1500 mm in length. A general layout of the soil-geosynthetic interaction device is presented in Fig. 2. As shown in Fig. 2a, normal stress was applied on soil specimens by six pneumatic actuators placed on wooden pyramids. These actuators reacted against a stiff reaction frame fixed to the bottom of the reinforced soil box. Axial loading was applied to active reinforcement specimens via a system of two hydraulic actuators reacting against the front wall of the soil box. As shown in Fig. 2b, two additional passive reinforcement layers of the same type were used as upper and lower boundaries to represent the presence of neighboring reinforcements. A combination of steel collars was used to control the reinforcement vertical spacing in different models. The soil-geosynthetic interaction device was developed to study potential load transfer amongst adjacent layers occurring when these layers deform differently

(Morsy, 2017; Zornberg et al. 2018; Morsy et al. 2019a, 2019b, 2020). The active reinforcement was attached to a loading system at its front end and was free at its rear end; whereas, the passive reinforcements were anchored at their rear ends. The experimental approach was developed to involve one reinforcement subject to active tension and two other neighboring reinforcements subject to passive tension. This signifies relative deformation of neighboring reinforcement layers. Such relative movement exists in a deformable reinforced soil system such as reinforced soil walls where reinforcements at different elevations strain differently causing load shedding amongst neighboring reinforcement layers. Additional details on the device can be found in Morsy (2017) and Morsy et al. (2019b).

3.2. Instrumentation and monitoring techniques

The soil-geosynethic interaction device was instrumented to monitor displacements in the geosynthetic reinforements and soil mass. The data used in the analyses conducted in this study were collected from the following instrumentation: (1) a load cell measuring the increasing tensile load applied to the active reinforcement; (2) a camera capturing the transparent sidewall, facilitating measurement of the soil displacement field as soil-reinforcement interaction was mobilized; (3) artifical gravel particles buried within the soil mass and connected to displacement sensors via horizontal telltales, which provided a comparison of displacements from internal particles with those obtained from particles adjacent to the transparent wall. These particles were made of hard plastic material and were shaped and sized to the average particle of the natural soil (Morsy et al., 2019b); (4) displacement sensors measuring displacements at numerous locations within the active reinforcement as well as within the passive reinforcements; and (5) a camera measuring displacements within the unconfined portion of the active reinforcement to evaluate the tensile behavior of the geosynthetic specimen used in the soil-geosynthetic interaction test.

3.3. Scope of the soil-geosynthetic interaction testing program

This section summarizes the soil-geosynthetic interaction tests (Morsy, 2017), which results were employed to conduct the analyses and develop the models presented in this paper. Table 1 presents a summary of the soil-geosynthetic interaction tests used in the development of the subsequent analytical model. As the table shows, the testing program included several testing series that explored the effects of various parameters on soil-reinforcement interaction. These series included repeatability assessment, varying normal stress levels for two
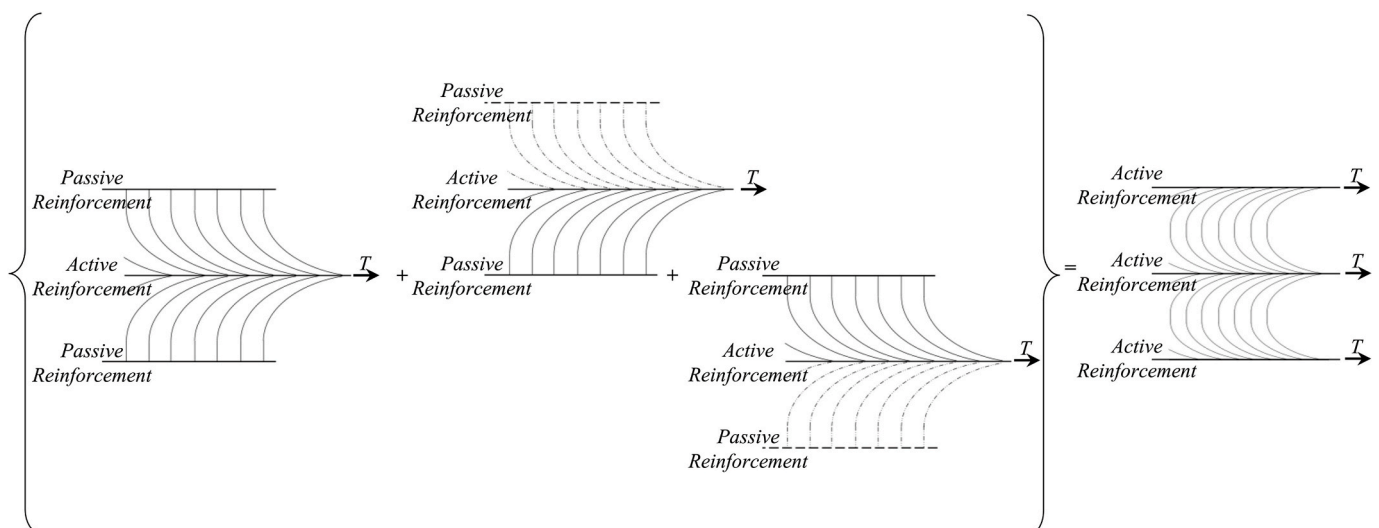

Fig. 1. Schematic representation of superposition to represent interaction among reinforcement layers within a reinforced soil system.
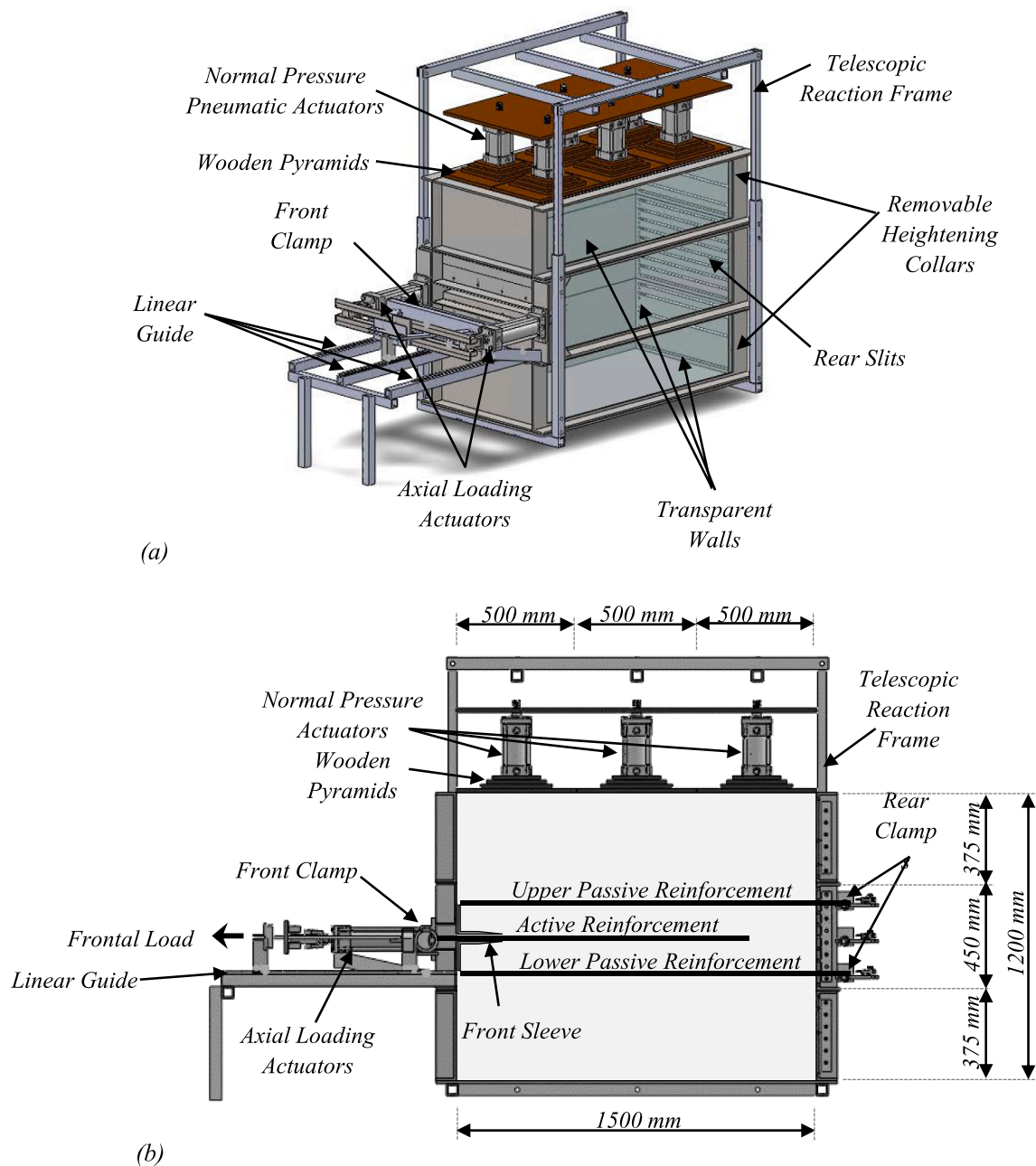
Fig. 2. Soil-geosynthetic interaction device: (a) general layout; and (b) schematic cross-sectional side view.

reinforcement spacings, varying reinforcement vertical spacings for three normal stress levels, and varying geosynthetic and soil types.

The baseline soil used in the soil-geosynthetic interaction tests was a pea gravel that conforms to AASHTO No. 8 gradation. The soil was placed dry at a relative density of 70%, which corresponds to a dry unit weight of 16.67 kN/m³ and a void ratio of 0.57. To achieve the target relative density, the soil was placed in lifts of controlled weights and volumes (Morsy, 2017; Morsy et al. 2019b). The angle of internal resistance at 70% relative density, obtained from triaxial testing, was 36.9° with a cohesion intercept of 15.6 kPa for a confining effective stress range of 35–105 kPa. Characteristic properties of the baseline soil (gravel) and the other soil type (sand) used in the soil-geosynthetic interaction testing program are summarized in Table 2.

The baseline reinforcement used in the soil-geosynthetic interaction tests was a polypropylene woven geotextile. The unconfined unit tension (ASTM D4595) reported by the geotextile manufacturer is 19.3, 39.4 and 70 kN/m at tensile strains of 2, 5 and 8%, respectively, in the cross-machine direction (direction used in the soil-geosynthetic interaction tests). These tensile properties were verified by test results obtained from monitoring the reinforcement tensile strain of the unconfined zone during testing, as detailed in Morsy (2017). Characteristic properties of the baseline geosynthetic and other geosynthetic types also used in the soil-geosynthetic interaction testing program are summarized in Table 3. These geosynthetic types include geogrids and geotextiles carefully selected to cover various geosynthetic characteristics (Morsy, 2017; Zornberg et al. 2018; Morsy et al. 2020). The study used the coefficient of soil-reinforcement interaction, C_i, which was found to provide a good collective indicator of the various mechanisms that take place between soils and reinforcements. Table 4 summarizes the coefficients of soil-reinforcement interaction, C_i, obtained for the various soil-reinforcement combinations used in the testing program, where C_i is commonly used to express the soil-reinforcement interaction

Table 1
Summary of soil-geosynthetic interaction tests used in this study (after Morsy, 2017).

Testing Scheme [1]	Test ID [2]	Testing Variables			
		Soil	S_v (m)	σ_v (kPa)	Reinforcements [3]
Repeat Tests	GP-04-07-G1-G	Gravel	0.10	50	W1-GT
	GP-04-07-G1-G(R)				
Tests with Varying Normal Stress Level	GP-06-02-G1-G	Gravel	0.15	15	W1-GT
	GP-06-03-G1-G			21	
	GP-06-05-G1-G			35	
	GP-06-07-G1-G			50	
	GP-04-03-G1-G	Gravel	0.10	21	W1-GT
	GP-04-07-G1-G			50	
	GP-02-03-G1-G	Gravel	0.05	21	W1-GT
	GP-02-07-G1-G			50	
Tests with Varying Reinforcement Vertical Spacing	GP-02-07-G1-G	Gravel	0.05	50	W1-GT
	GP-04-07-G1-G		0.10		
	GP-06-07-G1-G		0.15		
	GP-08-07-G1-G		0.20		
	GP-12-07-G1-G		0.30		
	GP-16-07-G1-G		0.40		
	GP-02-03-G1-G	Gravel	0.05	21	W1-GT
	GP-04-03-G1-G		0.10		
	GP-06-03-G1-G		0.15		
Tests with Varying Geosynthetic and Soil Types	GP-06-03-G1-G	Gravel	0.15	21	W1-GT
	GP-06-03-G2-G	Gravel			W2-GT
	GP-06-03-G4-G	Gravel			EX-GG
	GP-06-03-G5-G	Gravel			KN-GG
	SP-06-03-G1-G	Sand			W1-GT

Notes.
(1)Some tests are mentioned more than once in different testing schemes to show the extent of variation in each scheme.
(2)Test ID includes the following five components.
- Soil classification according to the Unified Soil Classification System (USCS)
- Reinforcement spacing S_v in inches
- Normal stress at the elevation of the active reinforcement in pounds per square foot
- Reinforcement number where G1 is W1-GT, G2 is W2-GT, G4 is EX-GG, and G5 is KN-GG
- Type of passive reinforcement where G signifies same type as active reinforcement
  (3)Reinforcement types are designations.
- W1-FT is woven geotextile #1
- W1-FT is woven geotextile #2
- EX-GG is extruded geogrid
- KN-GG is knitted geogrid

Table 2
Characteristics of soils used in soil-geosynthetic interaction tests.

Properties	Gravel	Sand
Name	Austin Washed Pea Gravel	Monterey Sand No. 30
Location	Austin, Texas	Monterey, California
Gradation	Poorly graded	Poorly graded
Particle Size Range, D	1.0–13.0 mm	0.2–2.0 mm
Mean Particle Size, D_{50}	7.0 mm	0.7 mm
Uniformity Coefficient, C_u	1.6	1.9
Curvature Coefficient, C_u	0.9	1.3
Specific Gravity, G_s	2.62	2.65
Range of Void Ratio, e_{min}-e_{max}	0.50–0.73	0.56–0.76
AASHTO Classification	A-1-a	A-3
USCS Classification	GP	SP
Particle Roundness	Sub-rounded to sub-angular	Rounded to sub-rounded
Mineral	Predominantly quartz	Predominantly quartz

Table 3
Characteristics of reinforcements used in soil-geosynthetic interaction tests.

Mechanical Properties	W1-GT (Cross-Machine Direction)	W2-GT (Cross-Machine Direction)	EX-GG (Cross-Machine Direction)	KN-GG (Machine Direction)
Ultimate tensile strength, T_{ult} (kN/m)	70.0	70.0	28.8	89.6
Tensile strength at 5% axial strain, $T_{@5\%}$ (kN/m)	39.4	70.0	19.6	45.7
Tensile stiffness, J (kN/m)	788	1400	392	914
Type	Woven Geotextile	Woven Geotextile	Extruded Biaxial Geogrid	Knitted Uniaxial Geogrid
Material	Polypropylene	Polypropylene	Polypropylene	Polyester

capacity can be expressed as follows:

$$C_i = \frac{\tan \phi_{sg}}{\tan \phi} \tag{1}$$

where ϕ_{sg} is the equivalent soil-reinforcement interface friction angle (i.e., friction angle as determined by pullout testing), and ϕ is the soil internal friction angle.

4. Representation of stress and strain fields

Based on the observations from soil-geosynthetic interaction experiments, analyses were conducted as part of the evaluation presented in this paper to model the displacements (and corresponding strains) both

Table 4
Soil-reinforcement interaction coefficients.

Soil-Reinforcement Combination	W1-GT/ Gravel	W2-GT/ Gravel	EX-GG/ Gravel	KN-GG/ Gravel	W1-GT/ Sand
C_i[a]	1.0	0.7	1.2[b]	1.5	1.1

[a] C_i: Soil-reinforcement interaction coefficient.
[b] An extrapolated value of ultimate tensile loading was used.

in the reinforcements and within the soil mass. The strains were subsequently used to predict the magnitude of load transfer from the reinforcements to the adjacent soil mass with increasing tension in reinforcements. A relevant assumption considered in these analyses was to consider that the impact of dilation is negligible when computing lateral soil strains with increasing shear stresses imposed in the soil-reinforcement interface. While the magnitude of dilation measured in the soil-geosynthetic interaction tests is small, dilation may have an effect on the state of stresses within the reinforced soil mass. To facilitate interpretation of the equations presented in the following sections, Fig. 3 illustrates the geosynthetic displacement, u_g, horizontal soil displacement, δ_s, and soil-geosynthetic relative displacement, δ_{sg}, as defined in the subsequent analyses. In addition, Fig. 4 illustrates the vertical normal stress in soil, σ_v, which varies in y direction; the horizontal normal stress in soil, σ_h, which varies in both x and y directions; the shear stress in soil, τ_s, which varies in x and y directions; the shear stress at soil-geosynthetic interface, τ_{sg}, which varies in x direction; and the tension in geosynthetic, T_g, which varies in x direction.

4.1. Displacement and strain fields

4.1.1. Reinforcement strains

In the soil-geosynthetic interaction tests, the reinforcement displacements, u_g, were measured at various locations along the reinforcement embedment length, L. The locations at which reinforcement displacements were monitored are shown in Fig. 5. Specifically, Fig. 5a, b, and 5c, respectively, show such locations on a plan view for the active reinforcement ($u1$ through $u10$ are respective points of $u_{g,u1}$ through $u_{g,u10}$ geosynthetic displacement measurements), upper passive reinforcement ($v1$ through $v5$ are respective points of $v_{g,v1}$ through $v_{g,v5}$ geosynthetic displacement measurements), and lower passive reinforcement ($w1$ through $w5$ are respective points of $w_{g,v1}$ through $w_{g,v5}$ geosynthetic displacement measurements). The figures also show the locations of the sleeve and rear boundary of the active reinforcement
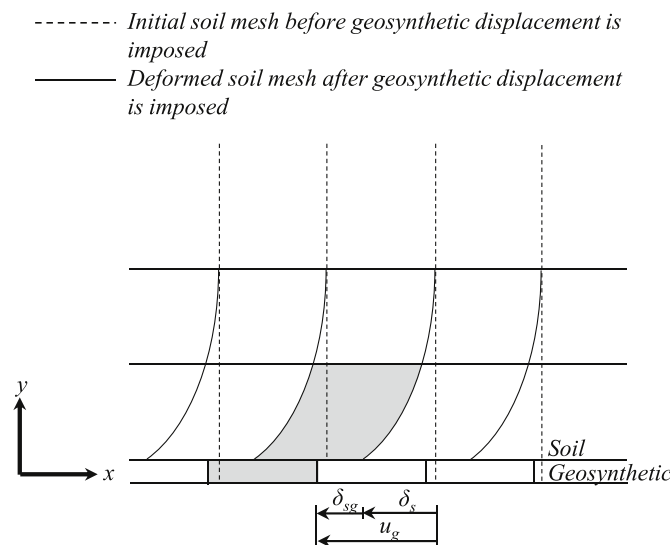
- - - - - - Initial soil mesh before geosynthetic displacement is imposed

———— Deformed soil mesh after geosynthetic displacement is imposed

Fig. 3. Schematic representation of reinforcement and soil displacements.

- - - - - - Initial soil mesh before geosynthetic displacement is imposed

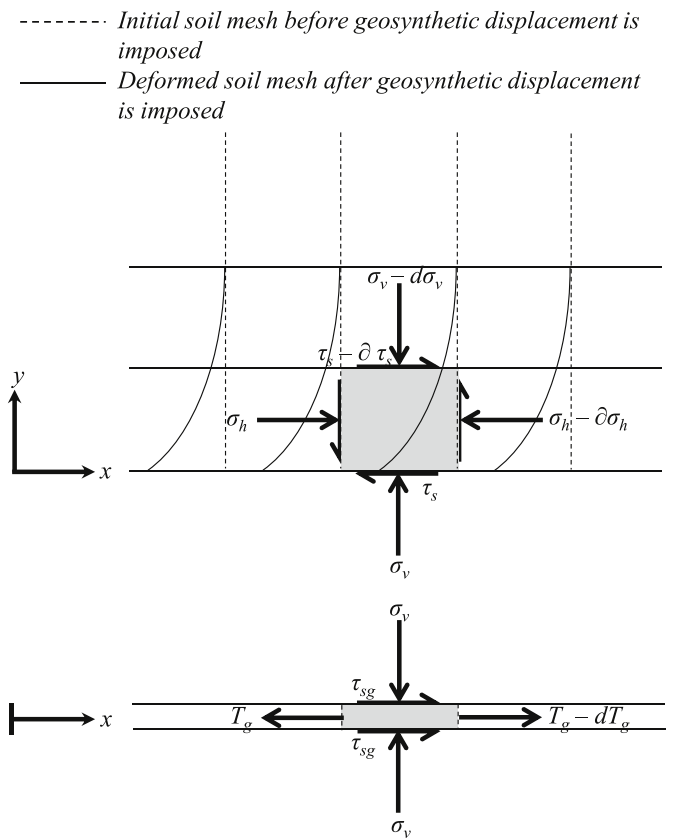*———— Deformed soil mesh after geosynthetic displacement is imposed*

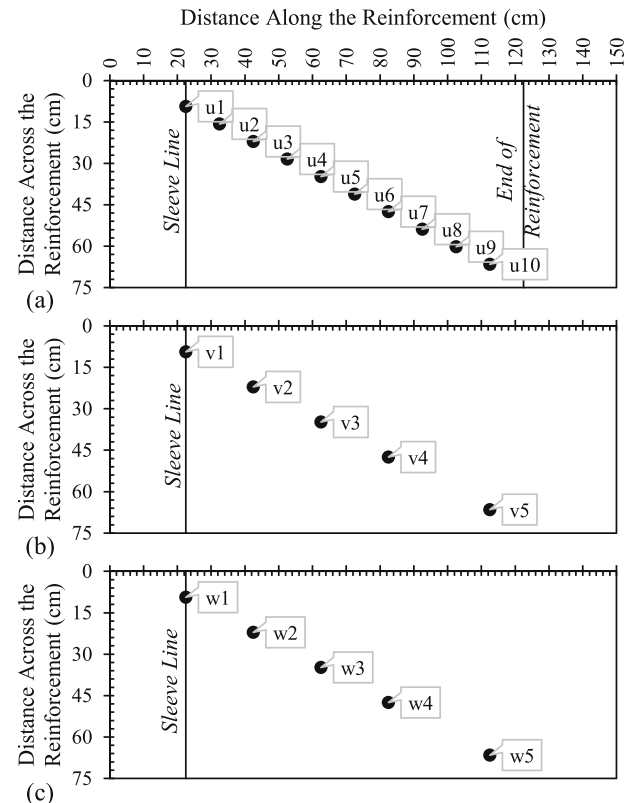**Fig. 4.** Schematic representation of reinforcement and soil stresses.

Fig. 5. Locations of telltale connections: (a) active reinforcement layer; (b) upper passive reinforcement layer; and (c) lower passive reinforcement layer.

layer.

The reinforcement displacement profile along the length of the reinforcement, $u_g(x)$, was modeled using an exponential function, which showed good fit with the experimentally obtained reinforcement displacements under increasing tensile loading. Specifically, the displacement magnitude was observed to decrease exponentially with increasing distance from the tensile loading front. Adopting an exponential decay to represent the displacements ensures a monotonic decrease in both displacements and tensile strain with increasing distance x from the tensile loading front. In the particular case of reinforcement displacements, the function was adopted to intercept the vertical axis (reinforcement displacement) at the location of the tensile loading front, $x = 0$. In other words, the y-intercept of the function corresponds to the reinforcement displacement at the loading front, $u_g(0)$. The reinforcement displacement function involves three parameters, A, B, and c, as follows:

$$u_g(x) = \frac{B}{e^{cx}} + A \qquad (2)$$

The parameter A represents the displacement asymptote corresponding to the displacement to which the farthest point in the reinforcement, $u_g(L)$, approaches. The asymptotic value is defined herein as $u_g(\infty)$, which represents a hypothetical reinforcement displacement at distance, x, approaching infinitum, ∞, that is:

$$A = u_g(\infty) \qquad (3)$$

The parameter B represents a multiplier that stretches the function as displacement progresses and is equivalent to the difference in reinforcement displacements between the y-intercept, $u_g(0)$, of the function and the horizontal asymptote, $u_g(\infty)$. Hence, the parameter B can be expressed as follows:

$$B = u_g(0) - u_g(\infty) \qquad (4)$$

The parameter c controls the curvature of the profile, which can be regarded as an indicator of the magnitude of soil-reinforcement interaction and is controlled by the various parameters affecting the soil-reinforcement interaction, including soil type, reinforcement type, and
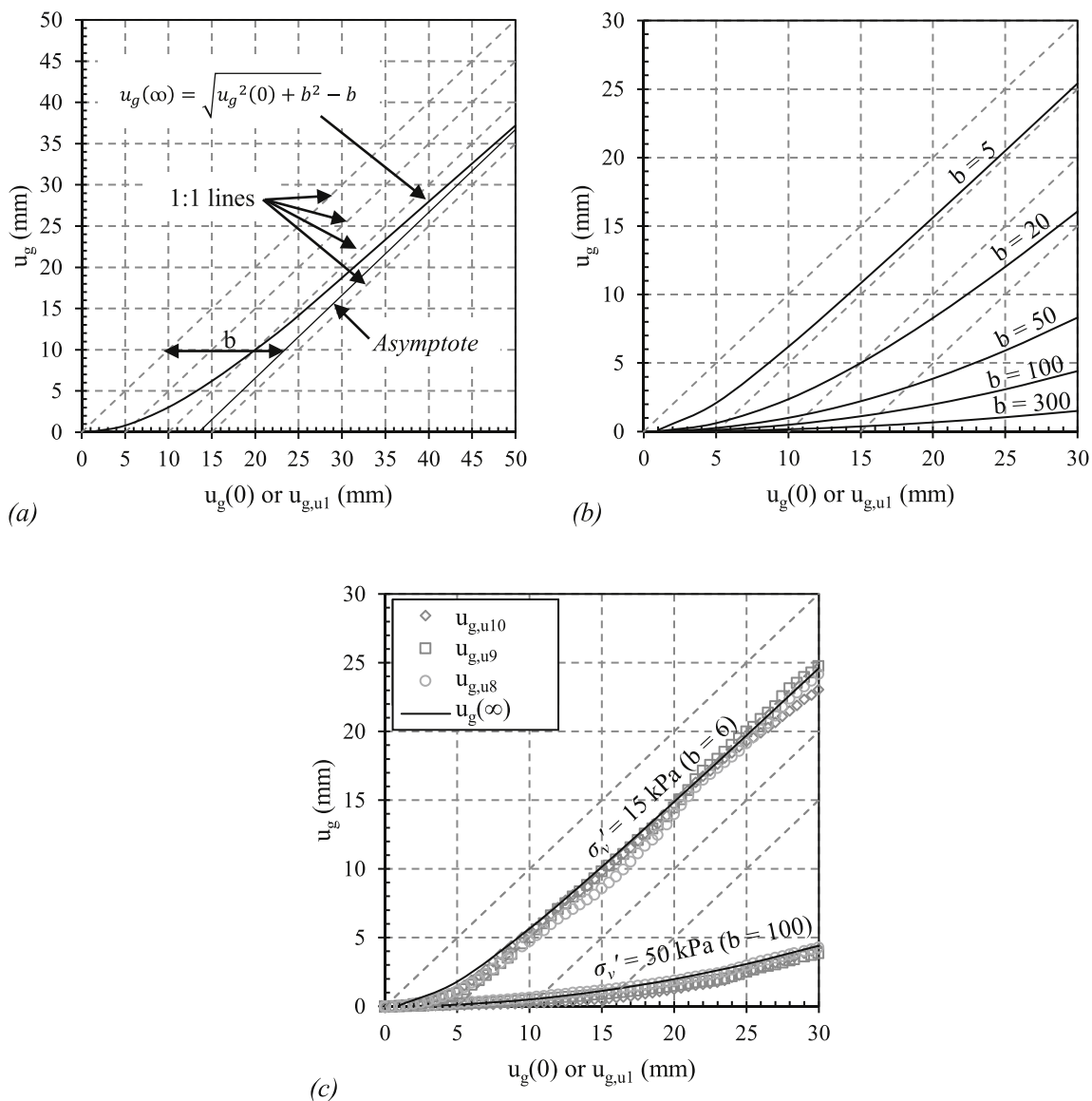

Fig. 6. Front versus rear reinforcement displacements: (a) schematic illustration; (b) variation of curvature coefficient, b; and (c) calibration with experimental results.

normal stress. Considering Eqn. (2) through (4), the reinforcement displacement function can be written as follows:

$$u_g(x) = \frac{u_g(0) - u_g(\infty)}{e^{cx/L}} + u_g(\infty) \qquad (5)$$

Note that the reinforcement length, L, is used to normalize the distance, x. The reinforcement displacement at an infinite distance, $u_g(\infty)$, can be approximated as being the same as the displacement at the rear of the reinforcement, $u_g(L)$; $u_g(L)$ can be determined at pullout failure, which is defined when the change in $u_g(L)$ with respect to $u_g(0)$ is 1.0 (*i. e.*, when the entire geosynthetic layer starts displacing as a rigid body, without further straining). The relationship between $u_g(L)$ and $u_g(0)$ can be expressed by a hyperbolic function with an asymptotic value for the slope $du_g(L)/du_g(0) = 1.0$.

$$u_g(\infty) = \sqrt{u_g{}^2(0) + b^2} - b \qquad (6)$$

where b is the curvature coefficient of the hyperbolic function, which controls the location of the asymptote to the hyperbolic function leg. Fig. 6a shows a schematic illustration of the hyperbolic model developed to predict $u_g(\infty)$, and Fig. 6b shows the sensitivity of the curvature coefficient, b, for values ranging from 5 to 300. As shown in Fig. 6b, the sensitivity of the $u_g(\infty)$ model to the curvature coefficient, b, decreases with increasing magnitude of b. For example, the difference between $u_g(\infty)$ values predicted for b of 100 and 300 is much smaller than that between $u_g(\infty)$ values predicted for b of 5 and 100. Fig. 6c shows comparisons between experimental data obtained from two tests, GP-06-02-G1-G and GP-06-07-G1-G, conducted with the same materials and using the same testing conditions, except for the normal stresses of 15 and 50 kPa, respectively (see Table 1 for testing condition details). The measured data shown in the figure correspond to the three different locations near the end of the reinforcement, where tensile strains remained negligible throughout most of the test (strains could be observed only for frontal loads beyond working values). It was concluded that the assumption of $u_g(\infty) = u_g(L)$ is reasonable and that $u_g(L)$ may not require iterations between the predicted and measured reinforcement displacements to converge.

Fig. 7 shows the predicted and measured reinforcement displacement profiles at various frontal displacements, $u_g(0)$, for test GP-06-07-G1-G (see Table 1 for testing condition details) using a curvature parameter, $c = 4$, and the hyperbolic curvature parameter $b = 100$ to deduce $u_g(\infty)$.

To examine the sensitivity of the curvature coefficients against the various testing variables, values of c and b were obtained for each test conducted in the experimental program. The curvature parameter of the displacement profile, c, used to fit the experimental results for the tests listed in Table 1 ranged from 2.5 to 5.5, with an average value of 4, which could practically be adopted as it resulted in adequate fit for the data from all tests. The curvature coefficient, c, is governed by several testing parameters that affect its value considerably, as follows: (1) the vertical normal stress, σ_v', (parameter c increases with increasing σ_v'); (2) the coefficient of soil-reinforcement interaction, C_i, (parameter c increases with increasing C_i); and (3) the reinforcement stiffness, J (parameter c decreases with increasing J). The testing database used in this study (Table 1) includes an adequate range of the aforementioned testing parameters. Since J and C_i both change with changing the reinforcement type, the ratio J/C_i was used collectively as one influencing parameter. Exponential relationships could be established between the curvature coefficient, c, and influencing testing parameters σ_v' and J/C_i as shown in Fig. 8a and b, respectively. The relationship can be expressed as follows:

$$c = 8.5 \left(\frac{\sigma_v'}{p_o} \right)^{0.33} \left(\frac{J}{C_i \, S_{ref} \, p_o} \right)^{-0.18} \qquad (7)$$

where p_o is the atmospheric pressure and S_{ref} is a reference reinforcement spacing equivalent to 1 m. Both p_o and S_{ref} were introduced into the equation for normalization. It should be noted that the relationship is dimensionally balanced and the curvature coefficient, c, is dimensionless. This function passes through the origin with $c = 0$ when $\sigma_v' = 0$ (*i.e.*, the reinforcement displacement profile is linear).

Similar to the curvature coefficient, c, the curvature coefficient, b, used to determine $u_g(\infty)$ was obtained for each test. The curvature coefficient, b, was found to be also governed by the same testing parameters as c (*i.e.*, σ_v', C_i, and J). Parameter b increases with increasing σ_v' and C_i, and decreases with increasing J. Exponential relationships could be established between the curvature coefficient, b, and influencing testing parameters σ_v' and J/C_i as shown in Fig. 8c and d, respectively. The relationship can be expressed as follows:

$$b = 3000 \left(\frac{\sigma_v'}{p_o} \right)^{2.5} \left(\frac{J}{C_i \, S_{ref} \, p_o} \right)^{-0.55} \qquad (8)$$

p_o and S_{ref} were introduced into the equation for normalization. The relationship passes through the origin where the value of b is zero, *i.e.*,
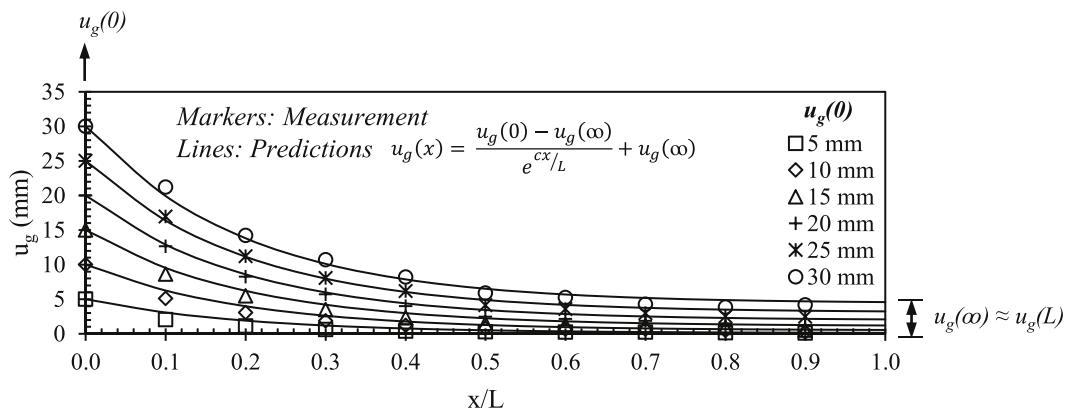

Fig. 7. Comparisons between measured and predicted reinforcement displacement profiles in a typical test (Test GP-06-07-G1-G) for frontal displacements ranging from 5 to 30 mm.

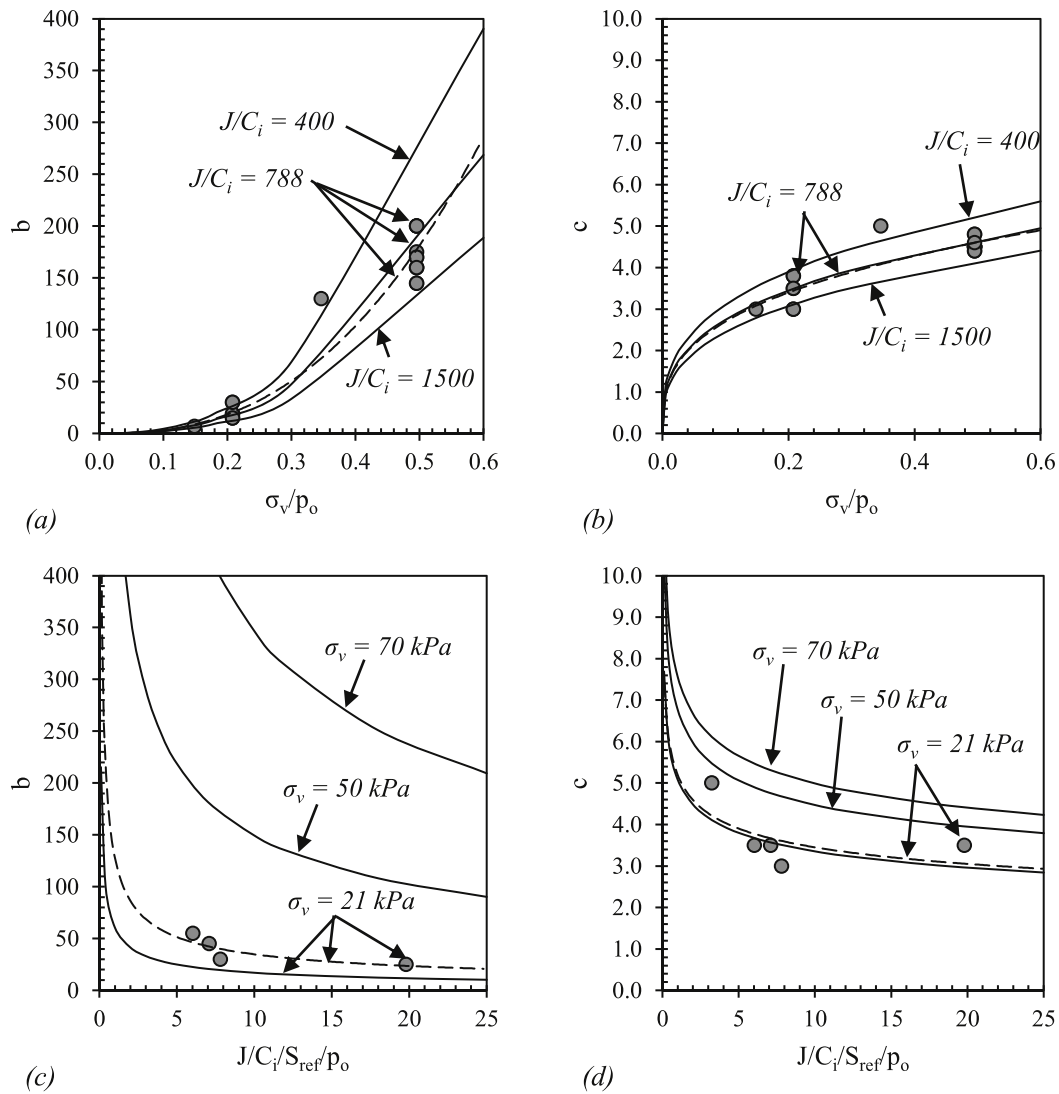Markers: Experimental Data
Dashed Lines: Best-Fit
Solid Lines: Model

Fig. 8. Reinforcement displacement curvature parameters: (a) normal stress dependency of curvature parameter c; (b) reinforcement properties dependency of curvature parameter c; (c) normal stress dependency of curvature parameter b; and (d) reinforcement properties dependency of curvature parameter b.

$u_g(\infty) = u_g(0)$ (no reinforcement straining), when the normal stress is zero. Note that the relationship is also dimensionally balanced and the curvature coefficient, b, is dimensionless.

The tensile strain, ε_g, can be predicted by differentiating the reinforcement displacement function with respect to x (distance along the reinforcement length). The strain ε_g can be written as a function of x as follows:

$$\varepsilon_g(x) = \left| \frac{[u_g(0) - u_g(\infty)]\,{}^c/_L}{e^{cx/_L}} \right|$$
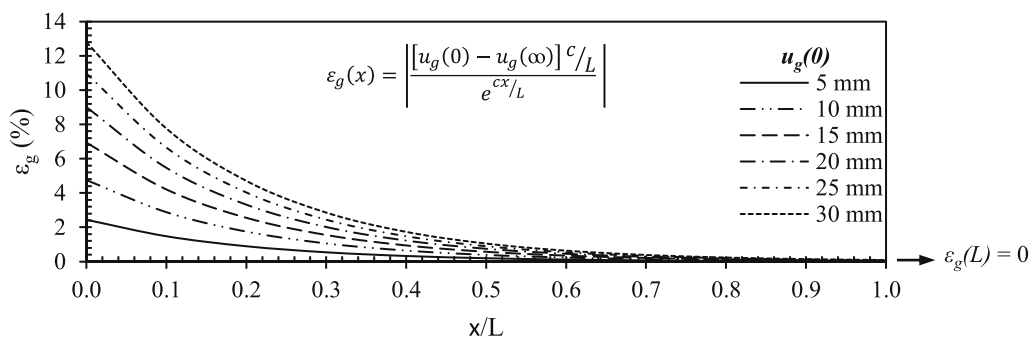
Fig. 9. Predicted reinforcement tensile strain profile in a typical test (Test GP-06-07-G1-G) for frontal displacements ranging from 5 to 30 mm.

$$\varepsilon_g(x) = \frac{du_g(x)}{dx} \qquad (9)$$

Hence,

$$\varepsilon_g(x) = \left| \frac{\left[u_g(0) - u_g(\infty)\right] \, c/L}{e^{cx/L}} \right| \qquad (10)$$

The tensile strain is expressed in an absolute form; however, tensile strains should be used with their respective signs per a consistent sign convention in reinforced soil systems involving analysis by super-position (*i.e.*, superposition of strains induced by different loading sources), as will be discussed later in this paper. Fig. 9 shows the pre-dicted reinforcement tensile strains obtained using the predicted rein-forcement displacement function.

4.1.2. Soil strains

Displacements within the reinforced soil mass were measured through the transparent side of the soil-geosynthetic interaction equip-ment, which allowed for direct visualization of the soil particles in a vertical section of the reinforced soil mass. Additionally, trackable artificial gravel particles, similar in size and shape to those of the gravel particles in the backfill material, were used to assess the accuracy of displacement measurements taken at the boundary wall of the rein-forced soil mass (Morsy, 2017; Morsy et al. 2019b). Fig. 10 shows the locations of the artificial gravel particles buried within the reinforced soil mass. Nine artificial gravel particles were stacked in a vertical line located 75 mm from the tensile loading front to measure horizontal displacements. Three artificial gravel particles were placed on top of the reinforced soil mass to measure vertical displacements.

Test results indicated that the relationship between the soil displacement, δ_s, measured adjacent to the soil-reinforcement interface (*i.e.*, maximum δ_s or $\delta_{s,max}$) and the reinforcement displacement, u_g, was approximately linear prior to reaching the ultimate interface shear strength. This observation was found to be valid for the various geo-synthetic reinforcement types used in this study, including geotextiles and geogrids, the various soil types and a reasonably wide range of normal stresses. A model involving key parameters that affect interface behavior was adopted to predict the soil displacement adjacent to the soil-reinforcement interface. One of these parameters is the soil-reinforcement interaction coefficient, C_i. The ratio between soil and geosynthetic displacements was found to correlate linearly with C_i, as illustrated in Fig. 11a. An additional parameter affecting soil displace-ments at the interface is the normal stress, σ_v', which was found to affect interface strength exponentially. Similar to shear modulus, a stress
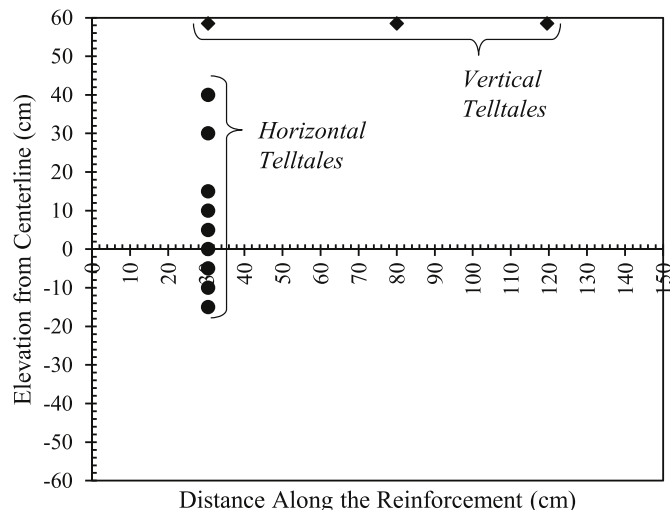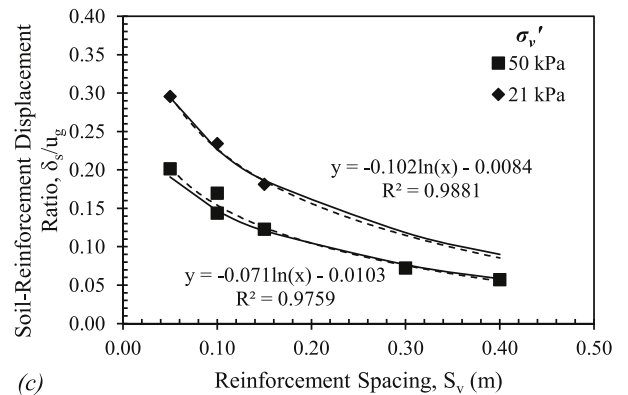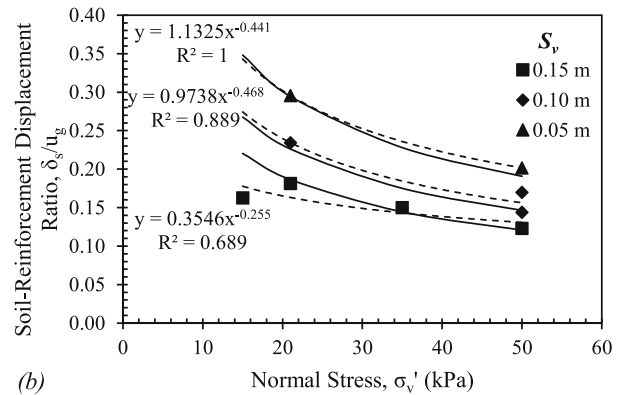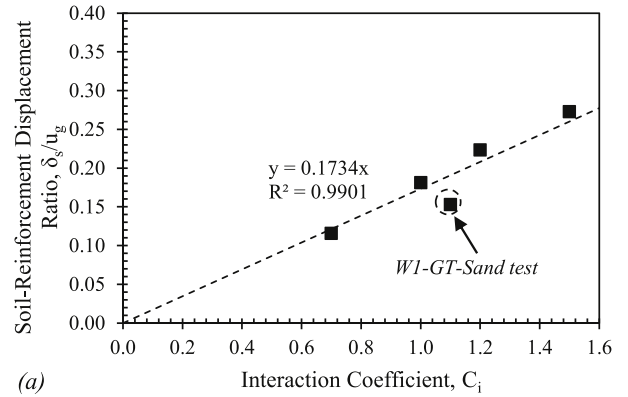

Fig. 10. Locations of artificial gravel particles within the reinforced soil mass.

Notes:
(1) Solid lines are for developed model
(2) Dashed lines are for best fit
(3) Equations are for best-fit lines

Fig. 11. Comparison between measured and predicted soil displacement next to the soil-reinforcement interface: (a) Effect of interaction coefficient; (b) Ef-fect of normal stress; and (c) Effect of reinforcement vertical spacing.

exponent, *n*, of 0.5 was adopted for the model and was found to adequately represent the effect of normal stress on the soil displacement at the interface, as shown in Fig. 11b. Finally, soil displacements were found to be affected by the reinforcement vertical spacing, S_v, which represents the presence of neighboring reinforcement layers in the vi-cinity of the soil-reinforcement interaction zone of the soil-reinforcement interface being evaluated. As discussed earlier, the concept of superposition was adopted to study the effect that loading an active reinforcement layer has on its neighboring passive layers. The results obtained from tests conducted with reinforcements placed at

different vertical spacings indicated that the presence of passive reinforcement layers affected the soil displacement adjacent to the soil-reinforcement interface, as well as the deformation pattern of the soil mass sandwiched in between the reinforcements (Morsy, 2017). The relationship between soil-reinforcement displacement ratio and S_v was found to follow a logarithmic function for various test groups of different normal stresses, as shown in Fig. 11c.

The soil displacements used in the development of these correlations were measured near the loaded front of the active reinforcements at x/L of 0.075, at mid-width of the soil mass, using artificial gravel particles adjacent to the active reinforcement layer. Additional redundant displacement measurements were obtained via digital imaging from the transparent sidewall of the reinforced soil box. However, confidence in the measurements obtained near the soil-reinforcement interface using the artificial gravel particles was higher than those obtained using digital imaging because of potential particle rotations and significant pattern distortions that took place close to the soil-reinforcement interface, especially at large loading levels. These rotations, including those parallel, oblique, and normal to the transparent wall, as well as pattern distortions reduced the accuracy and ability to gather soil displacements via digital images.

Based on the correlations developed to quantify the effect of different key parameters on the soil-reinforcement interface behavior, a model was developed to predict soil displacements adjacent to the soil-reinforcement interface as a function of the displacements in the geosynthetic reinforcement. The proposed model can be expressed as follows:

$$\delta_{s,max}(x) = C_i \left(\frac{\sigma_v{}'}{p_o}\right)^{-n} \ln\left(\frac{S_{v,ref}}{S_v}\right)^m u_g(x) F(x) \tag{11}$$

where

$$\delta_{s,max}(x) = \delta_s(x, 0) \tag{12}$$

where C_i is the soil-reinforcement interaction coefficient, n is a stress exponent, m is a vertical spacing exponent, p_o is the atmospheric pressure, which is introduced to the equation for normalization, $S_{v,ref}$ is a dimensionless factor used to normalize reinforcement vertical spacing, being defined as 1.0 m, and $F(x)$ is a dimensionless empirical factor that accounts for potential changes in the ratio between soil displacements next to the interface, $\delta_{s,max}$, to reinforcement displacements, u_g.

The constant n can be regarded as the dependency of soil-reinforcement interface shear resistance to the normal stress. The value of n was evaluated empirically as 0.5, which is within the typical range of stress exponent values used to express the stress dependency of soil shear strength (*e.g.*, Mitchell and Soga, 2005). The constant m was evaluated empirically to be 0.045. The recommended value for this exponent was obtained after model calibration against the experimental data obtained from the soil-geosynthetic interaction tests listed in Table 1. While the testing program involved a wide range of reinforcement and soil combinations (*i.e.*, material combinations with wide-ranging soil-reinforcement interaction coefficients, from 0.7 to 1.5), this exponent may require refinement for soil and reinforcement combinations other than those considered in the experimental testing program. It should be noted, however, that the baseline soil and reinforcement combination used in the experimental program listed in Table 1 (Morsy, 2017) had an interaction coefficient, C_i, of 1.0 and involved soil and reinforcement types that have been widely used in geosynthetic-reinforced soil structures (Adams et al. 2011; Zornberg et al. 2018).

The parameter $F(x)$ accounts for potential changes in the ratio between $\delta_{s,max}$ and u_g. This factor equals unity at the loading front (*i.e.*, $F(0) = 1.0$) may decrease along the reinforcement length. $F(x)$ can be determined by back-calculation when both soil and reinforcement displacements are known. These displacements were determined from results of the tests listed in Table 1 (Morsy, 2017) during which the soil

displacement at the interface, $\delta_{s,max}$, was monitored both by digital imaging along the reinforcement length and artificial gravel particles at a point near the loading front. Soil displacements, $\delta_{s,max}$, along the reinforcement length can be determined from analysis of digital images tethered during testing. Alternatively, the soil shear modulus, G, can be calculated at a single point near the reinforcement loading front, which is monitored by the artificial gravel particles.

Knowing the shear modulus, G, of the fill material under the testing conditions (*i.e.*, for a given normal stress and void ratio) allows predicting the soil shear strain at the interface, γ_s, along the reinforcement length. Therefore, the soil displacement at the interface, $\delta_{s,max}$, can be determined along the reinforcement length if the interface shear stress, τ_{sg}, is known. Specifically, the parameter $F(x)$ could be calibrated by warranting a constant shear modulus, G, along the reinforcement length, which is presented later in the paper following an introduction of the calculation of soil shear strains. Note that G could be calculated accurately at location $x/L = 0.075$ and then used to precisely back-calculate the parameter $F(x)$. For highly curved reinforcement displacement profiles (values of curvature coefficient b greater than 100), this parameter was found to approximately follow a simple linear relationship, as follows:

$$F(x) = \left(1 - \frac{x}{L}\right) \tag{13}$$

Fig. 12 shows the predicted and measured soil displacement profiles adjacent to the soil-reinforcement interface, $\delta_{s,max}$, at various frontal displacements, $u_g(0)$. Note that the soil displacement prediction adjacent to the soil-reinforcement interface presented in Fig. 12 was developed using data obtained the trackable artificial gravel particles at x/L of 0.075.

While parameter $F(x)$ is indicated in Eqn. (11) for completeness, only the soil displacement at the reinforcement loading front ($x = 0$), where $F(0) = 1.0$, is relevant to this study. Design methods for retaining walls typically consider that the locus of maximum reinforcement tension corresponds to the location of the critical failure surface within the reinforced soil mass. Fig. 13a shows a typically assumed reinforcement tension profile along reinforcement layers in a reinforced soil wall. The location of the maximum reinforcement tension in a road base stabilized with geosynthetics is shown in Fig. 13b. With the objective of simulating practical cases like those in Fig. 13, the soil displacements next to the interface near the reinforcement loading front ($x/L = 0.075$) were measured in the tests listed in Table 1 using artificial gravel particles and verified by data obtained through digital imaging to considerable strain levels (Morsy et al. 2019a).
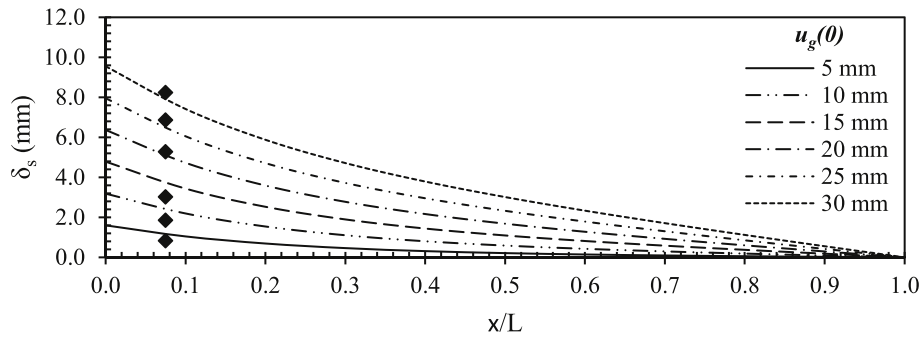
Soil displacements decrease with increasing the distance from the soil-reinforcement interface. The horizontal soil displacement profile was found to be adequately represented using an exponential function. A suitable prediction model was identified as follows:

$$\delta_s(x, y) = \frac{\delta_{s,max}(x, y)}{e^{fy/y_{cr}}} \tag{14}$$

where y_{cr} is a critical distance adopted for normalization and equals 0.3 m, which was observed in the soil-geosynthetic interaction tests to be a reasonable boundary where the induced shear strains tend to zero (Morsy, 2017; Zornberg et al. 2018, 2019; Morsy et al. 2019a). The critical distance y_{cr} also corresponds to the distance specified by ASTM D6706 (2013) at which the top and bottom boundaries of the soil have insignificant effects during testing for ultimate pullout resistance. The constant f is a curvature parameter that depends on the shear stiffness of the soil.

The shear strain in the soil can be obtained by differentiating the soil displacement function in relation to the direction normal to the soil-reinforcement interface, as follows:

$$\gamma_s(x, y) = \frac{\partial \delta_s(x, y)}{\partial y} \tag{15}$$

Fig. 12. Horizontal soil displacement profile at various frontal displacements of the active reinforcement, u_g (0).
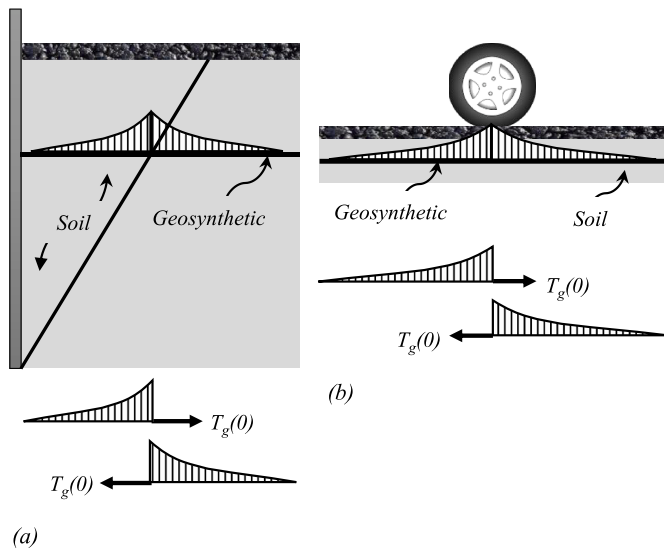

Fig. 13. Typical tensile stress distribution along a reinforcement layer in a reinforced soil system: (a) geosynthetic-reinforced soil wall; and (b) road base stabilized with geosynthetic.

Then,

$$\gamma_s(x,y) = \left| \frac{\delta_{s,max}(x) f/y_{cr}}{e^{fy/y_{cr}}} \right| \qquad (16)$$

The soil shear strain in Eqn. (16) is expressed in an absolute form. However, shear strains should be used with their respective sign per a consistent sign convention in reinforced soil systems involving the superposition of shear strains induced by different soil-reinforcement interfaces, as will be discussed later in this paper. Fig. 14a shows a comparison between predicted and measured soil horizontal displacement profiles at increasing values of frontal displacement, $u_g(0)$, obtained from test GP-16-07-G1-G (see Table 1 for testing condition details). The curvature parameter, f, used to fit this particular test (testing conditions) was 1.0. Fig. 14b illustrates the soil shear strains obtained based on the predicted soil horizontal displacements.

The curvature parameter of the soil displacement profile, f, used to fit the testing data in this study (Table 1) ranged between 1.2 and 3.0, with an average value of 2.2, which was found to adequately fit the data obtained for all tests. No clear trend could be found between the f and
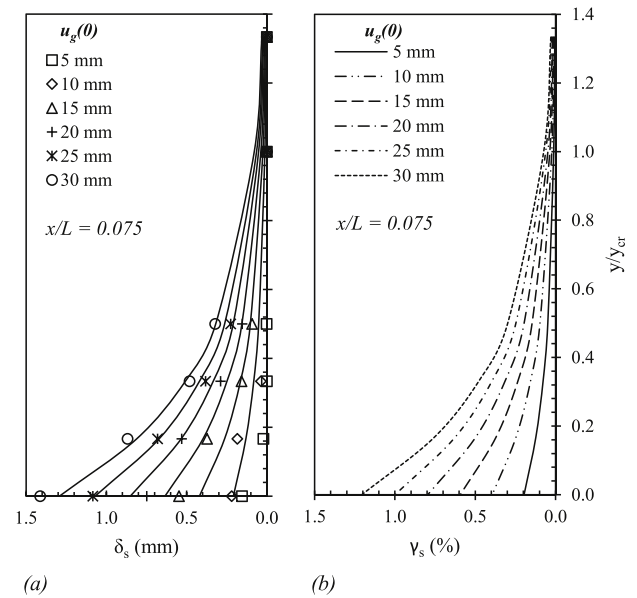

Fig. 14. (a) Measured versus predicted soil displacement normal profiles; and (b) soil shear strain profile.

other testing conditions (reinforcement vertical spacing, reinforcement type, and soil type) within the testing database used in this study (Table 1). Consequently, an f value of 2.2 is recommended in the absence of test data.

4.1.3. Soil-reinforcement relative displacement

An understanding of the soil-reinforcement interface shear is relevant to properly model its mechanical behavior under both working and ultimate stress conditions. The relative displacement is defined as the difference between the displacements of the reinforcement and those of the adjacent soil (i.e., reinforcement slippage out of the surrounding soil). Soil-reinforcement interface shear has often been modeled considering that the interface shear mobilization is a function of the relative soil-reinforcement displacements along the interface. Since soil displacements are generally not measured or known, such relative displacement has often been assumed in interaction tests to equal the reinforcement displacement (i.e., assuming that soil is stationary). However, results from the soil-geosynthetic interaction tests reported by Morsy (2017) and Morsy et al. (2019a, 2019b, 2020) revealed that the displacements of the soil adjacent to the soil-reinforcement interface are

actually not negligible. Accordingly, soil-reinforcement relative displacement, δ_{sg}, in this study was obtained by subtracting the soil displacement, δ_s, at the interface from the reinforcement displacement, u_g, at the same location, as follows:

$$\delta_{sg}(x) = u_g(x) - \delta_{s,max}(x) \tag{17}$$

Then, considering Eqn. (11), the soil-reinforcement relative displacement can be predicted as follows:

$$\delta_{sg}(x) = \left[1 - C_i\left(\frac{\sigma_v{}'}{p_o}\right)^{-n}\ln\left(\frac{S_{v,ref}}{S_v}\right)^m F(x)\right] u_g(x) \tag{18}$$

4.2. Stress fields

4.2.1. Reinforcement stresses

The reinforcement unit tension (*i.e.*, tensile force per unit width of the reinforcement), T_g, can be determined by multiplying the reinforcement tensile strain and its tensile stiffness, J, as follows:

$$T_g(x) = J\varepsilon_g(x) \tag{19}$$

Hence, considering Eqn. (10),

$$T_g(x) = J\left|\frac{[u_g(0) - u_g(\infty)]\,c/L}{e^{cx/L}}\right| \tag{20}$$

4.2.2. Soil-reinforcement interface shear stresses

The relationship between the reinforcement unit tension, T_g, and the corresponding soil-reinforcement interface shear stress, τ_{sg}, mobilized at the same location, x, can be obtained from equilibrium, as follows:

$$dT_g(x) = 2\,\tau_{sg}(x)\,dx \tag{21}$$

Or,

$$\tau_{sg}(x) = \frac{1}{2}\frac{dT_g(x)}{dx} \tag{22}$$

Considering Eqn. (19),

$$\tau_{sg}(x) = \frac{J}{2}\frac{d\varepsilon_g(x)}{dx} \tag{23}$$

Then, considering Eqn. (9),

$$\tau_{sg}(x) = \frac{J}{2}\frac{d^2 u_g(x)}{dx^2} \tag{24}$$

Therefore, considering Eqn. (10),

$$\tau_{sg}(x) = \frac{J}{2}\left|\frac{[u_g(0) - u_g(\infty)]\left(c/L\right)^2}{e^{cx/L}}\right| \tag{25}$$

4.2.3. Soil stresses

Fig. 15 illustrates the state of stresses within the soil mass adjacent to an active reinforcement layer in a soil-geosynthetic interaction test. Specifically, Fig. 15a shows the distortion in the principal stress planes upon generation of shear stresses at the soil-reinforcement interface, which eventually results in load transfer to the reinforcement (Wang et al. 2016; Morsy, 2017). The figure also presents a schematic of the state of stresses on a soil element adjacent to the interface and the corresponding Mohr's circle representation of the state of stresses. Fig. 15b presents a schematic of the difference in the states of stresses for three soil elements: (1) near the soil-reinforcement interface; (2) away from the soil-reinforcement interface and within the zone of shear influence; and (3) away from the soil-reinforcement interface and outside the zone of shear influence. The figure also displays the corresponding Mohr's circle representations of the states of stresses of the three soil elements, which take into account the variation of vertical stress (*i.e.*, overburden stress and any added surcharge) with depth.

The shear stress-strain relationship of the soil can be written as follows:

$$\tau_s(x, y) = G\gamma_s(x, y) \tag{26}$$

where G is the shear modulus of the soil and can be obtained using the boundary condition adjacent to the soil-reinforcement interface, as follows, where the τ_s is equal to τ_{sg}:

$$\tau_s(x, 0) = \tau_{sg}(x) = G\gamma_s(x, 0) \tag{27}$$

Therefore, the shear modulus, G, can be obtained at various locations along the reinforcement length. Fig. 16 shows the shear stress-strain relationship for test GP-16-07-G1-G, which is representative of that obtained for the other tests (see Table 1 for testing condition details). As the figure confirms, the shear stress-strain curves predicted at various locations along the reinforcement are in good agreement (*i.e.*, predicted shear moduli are in good agreement), which validates the prediction procedure. It should be noted that the shear modulus, G, degrades with increasing shear strain. This degradation is stress-dependent and was observed to be more significant in tests conducted under comparatively low normal stresses. As previously discussed, the parameter $F(x)$ (in Eqn. (11)) could be determined using this information.

By studying the state of stresses on a differential element located at distance x from the tensile loading front and a distance y from the soil-reinforcement interface, instant-equilibrium equations can be written along the direction of the major principal stress, σ_1, as follows:

$$\sigma_1(x, y)dx \cos\theta(x, y) = \sigma_v(y)dx \cos\theta(x, y) + \tau_s(x, y)dx \sin\theta(x, y) \tag{28}$$

This equation can be written in a simplified form, as follows:

$$\sigma_1(x, y) = \sigma_v(y) + \tau_s(x, y)\tan\theta(x, y) \tag{29}$$

Similarly, instant-equilibrium equations can be written along the direction of the minor principal stress, σ_3, as follows:

$$\sigma_3(x, y)dx \sin\theta(x, y) = \sigma_v(y)dx \sin\theta(x, y) - \tau_s(x, y)dx \cos\theta(x, y) \tag{30}$$

This equation can also be written in a simplified form, as follows:

$$\sigma_3(x, y) = \sigma_v(y) - \tau_s(x, y)\cot\theta(x, y) \tag{31}$$

The ratio between principal stresses, N, can be expressed in terms of the soil internal friction angle, ϕ, as follows:

$$N = \frac{\sigma_1}{\sigma_3} = \tan^2\left(45 + \frac{\varphi}{2}\right) \tag{32}$$

Considering Eqn. (29) and (31),

$$N = \frac{\sigma_v(y) + \tau_s(x, y).\tan\theta(x, y)}{\sigma_v(y) - \tau_s(x, y)\cot\theta(x, y)} \tag{33}$$

This equation can be simplified and a quadratic equation can be written for the tangent of the angle of principal stress inclination, θ, as follows:

$$\tau_s(x, y)\tan^2\theta(x, y) + (1 - N)\sigma_v(y)\tan\theta(x, y) + N\tau_s(x, y) = 0 \tag{34}$$

where the solution to this equation defines the angle of principal stress inclination as follows:

$$\theta(x, y) = \tan^{-1}\left[\frac{(N - 1)\sigma_v(y) \pm \sqrt{(N - 1)^2\sigma_v{}^2(y) - 4N\tau_s{}^2(x, y)}}{2\tau_s(x, y)}\right] \tag{35}$$

The angle of principal stress inclination, θ, increases with increasing shear stresses at the soil-reinforcement interface. The horizontal normal stress, σ_h, can then be deduced by determining the vertical earth pressure at a given reinforcement layer, σ_v, using the following relationship:

$$\sigma_h(x, y) = \sigma_1(x, y) + \sigma_3(x, y) - \sigma_v(y) \tag{36}$$

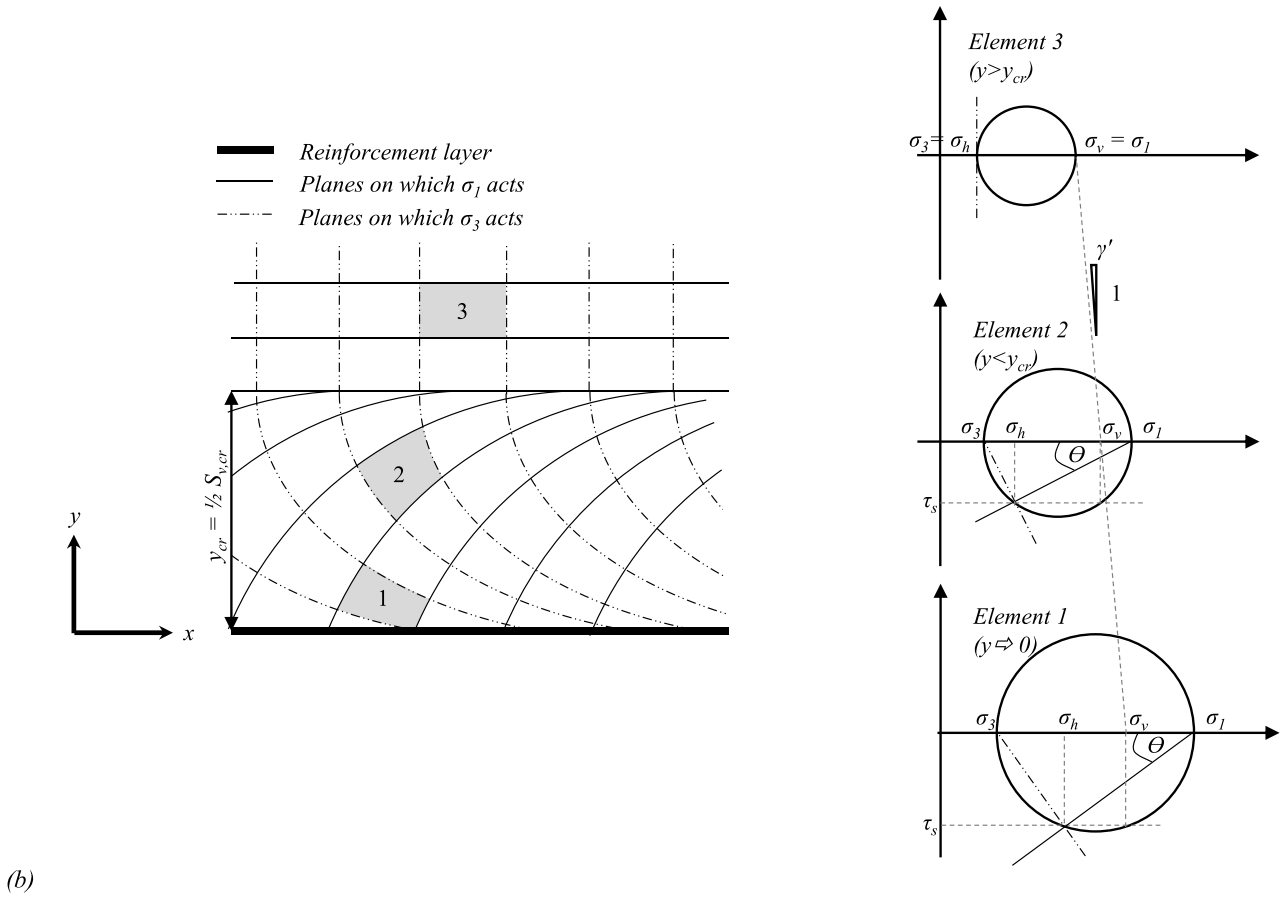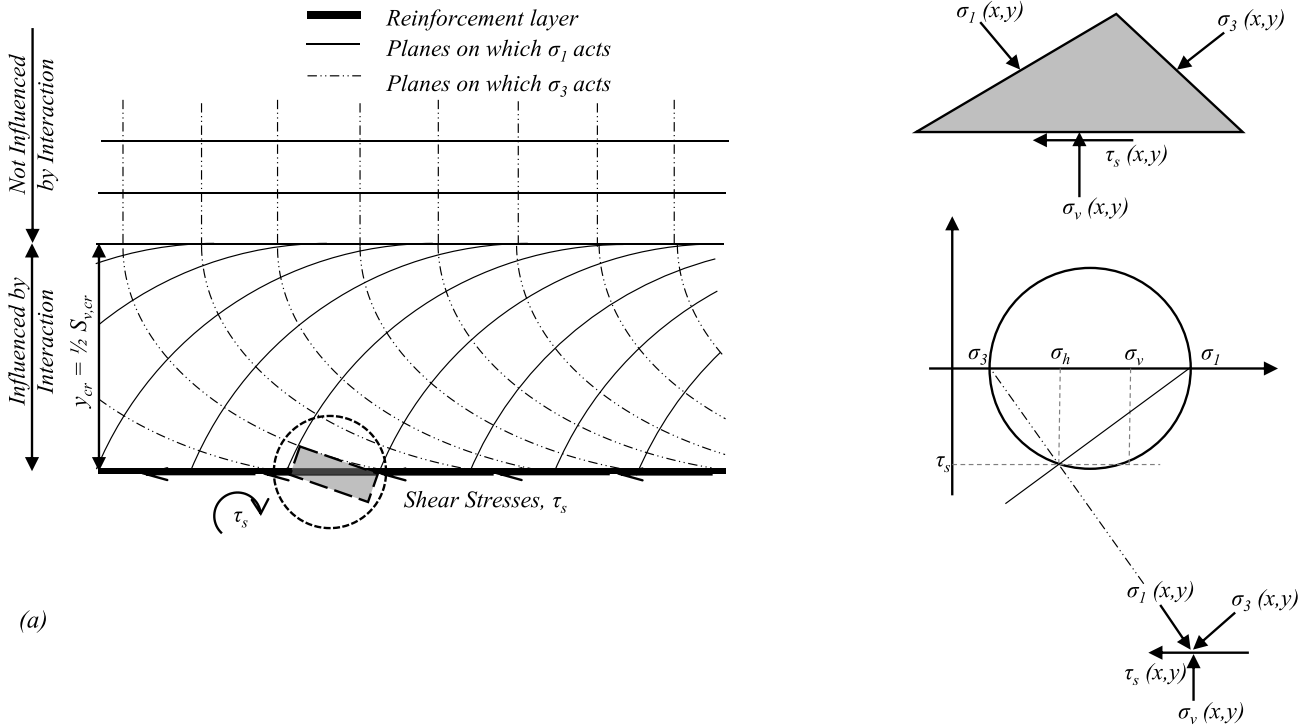The coefficient of lateral earth pressure, K_h, at any point x,y is

Fig. 15. State of stresses: (a) at soil-reinforcement interface; and (b) away from soil-reinforcement interface.
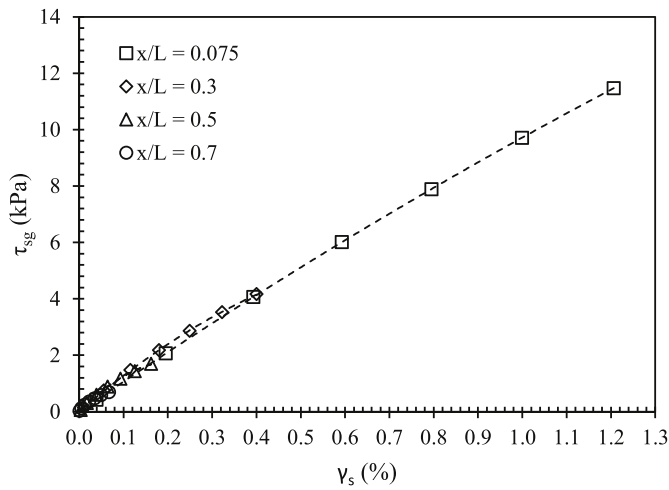
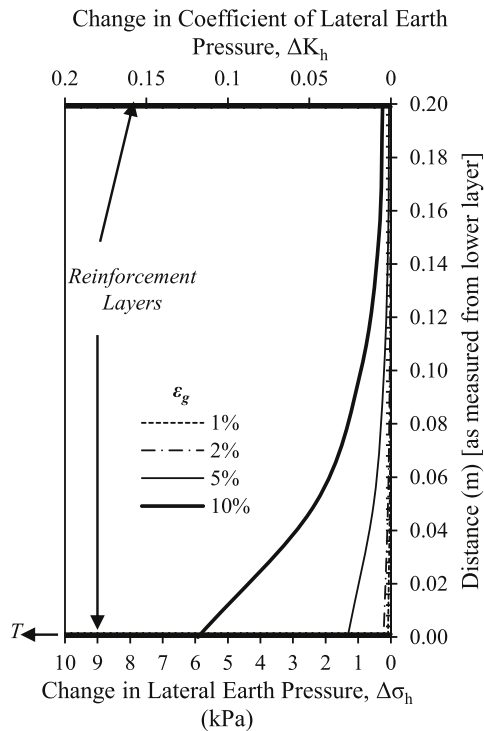**Fig. 16.** Soil shear stress-strain relationships.

Fig. 17. Change in lateral earth pressure at various reinforcement strain levels in a typical test (Test GP-02-07-G1-G).

defined as follows:

$$K_h(x,y) = \frac{\sigma_h(x,y)}{\sigma_v(y)} \tag{37}$$

Fig. 17 shows the effect of soil-reinforcement interaction on lateral earth pressure with increasing distance from soil-reinforcement interface, and at various reinforcement strain levels for test GP-02-07-G1-G.

5. Interaction of soil-reinforcement composites in a reinforcement group

The term "composite" has been used in the context of reinforced soil in several previous studies, although bearing different meanings. An early definition refers to the individual reinforcement scale (unit-reinforcement scale), where the term "soil-reinforcement composite" was used to refer to the composite comprised of an individual reinforcement layer and the adjacent soil (Werner and Resl, 1986). A similar definition was used by Zornberg et al. (2017) to define a soil-reinforcement interaction parameter termed "soil-reinforcement composite stiffness." Subsequently, Morsy (2017) used the term "soil-reinforcement composite" to refer to an individual reinforcement layer and the adjacent soil of a thickness equivalent to the extent of shear stress transfer. The second definition refers to the reinforced soil mass global scale (multiple-reinforcement scale), while the term "composite reinforced soil mass" was used to refer to a reinforced soil mass acting globally as a unit composite mass (*e.g.*, Holtz and Lee, 2002; Adams et al. 2011; Wu et al. 2013; Nicks et al. 2013). Additionally, the term "reinforced soil composite behavior" was defined by Zornberg et al. (2018, 2019) as the response of reinforced soil structures that results when loading of a geosynthetic reinforcement affects the deformation response and load magnitude of adjacent reinforcement layers.

The "composite behavior of a reinforced soil system" (global) can be achieved when interaction takes place among individual soil-reinforcement composites (local). As previously discussed in this paper, the interaction among neighboring reinforcement layers was studied by superposition of the load transfer resulting from each individual active reinforcement. It should be noted that the load transfer among reinforcement layers takes place through the in-between soil layers. In cases involving multiple active reinforcements, load transfer into a soil layer occurs at the soil-reinforcement interfaces of two reinforcement layers. Consequently, the analytical solutions developed for stresses in a reinforced soil mass with individual active reinforcement layers were used to develop solutions for stresses developing in reinforced soil masses with groups of active reinforcement layers. Solutions presented in this paper include reinforced soil masses with two active reinforcement layers at various vertical spacings.

Fig. 18a and b displays schematics of the stress interaction between the shear stress influence zones for two neighboring reinforcement layers within their in-between soil layer in largely-spaced and closely-spaced reinforced soil systems, respectively. As presented in Fig. 18a, if the reinforcement spacing is large enough for the shear stress zones not to interfere, the reinforcement layers will behave independently (*i.e.*, no or negligible interaction occurs among reinforcements). In this condition, the reinforcement spacing is larger than the critical reinforcement spacing, $S_{v,cr}$, and no composite behavior appears on the reinforced soil mass. In contrast, as shown in Fig. 18b, if the reinforcement spacing is small enough for the shear stress zones to interfere, the reinforcement layers will behave as a group (*i.e.*, interaction occurs among reinforcements). The interaction among reinforcement layers increases with decreasing reinforcement spacing. In this case, the reinforcement spacing is smaller than the critical reinforcement spacing, $S_{v,cr}$, and a composite behavior dominates on the reinforced soil mass.

Considering Eqn. (25) and (16), the shear stresses resulting within a soil layer sandwiched between two reinforcement layers placed at a vertical spacing S_v can be written as follows:

$$\tau_s(x,y) = \sum_{i=1}^{2} \tau_{s,i}(x,y) = \left| \frac{\delta_{s,max}(x) f/y_{cr}}{e^{fy_1/y_{cr}}} \right| - \left| \frac{\delta_{s,max}(x) f/y_{cr}}{e^{fy_2/y_{cr}}} \right| \tag{38}$$

where y_1 and y_2 are the absolute distance away from reinforcement layers 1 and 2, respectively, as shown in Fig. 18. Hence,
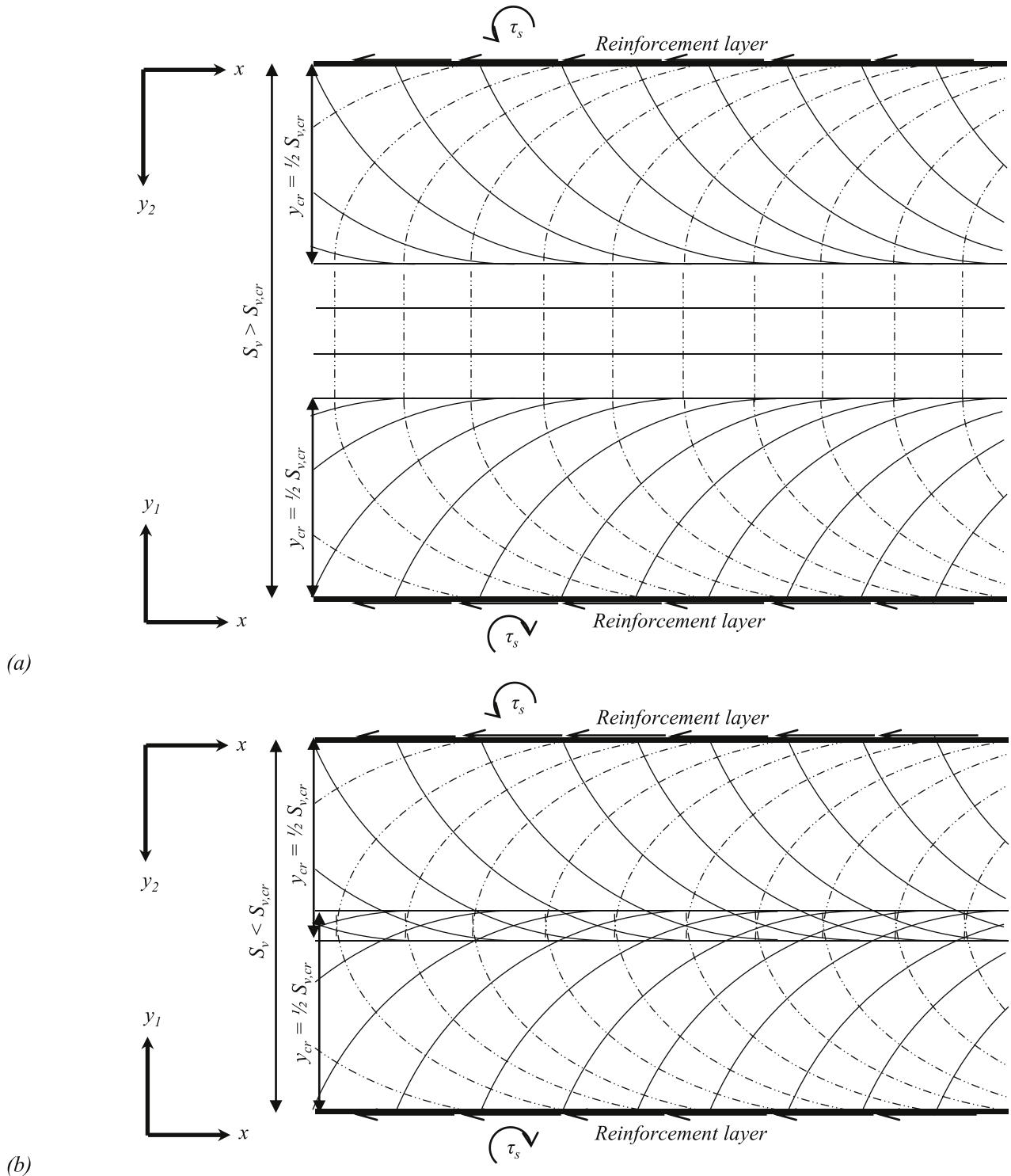
$$y_1 + y_2 = S_v \tag{39}$$

Fig. 18. Interaction of soil-reinforcement composites: (a) no overlap of influence zones; and (b) overlap of influence zones.

Note that shear stresses generated from different reinforcements follow different directions, as illustrated in Fig. 18. The superposition between the stresses induced in a soil layer sandwiched between two tensioned reinforcement layers allows evaluating the effect of reinforcement vertical spacing on the state of stresses in reinforced soil structures. For instance, Fig. 19 presents a comparison between the change in lateral earth pressure profiles for three soil layers of different thicknesses (*i.e.*, different reinforcement vertical spacings). Specifically, Fig. 19a through 19c show the change in lateral earth pressure for reinforcement spacings of 0.2, 0.4 and 0.6 m, respectively, at various
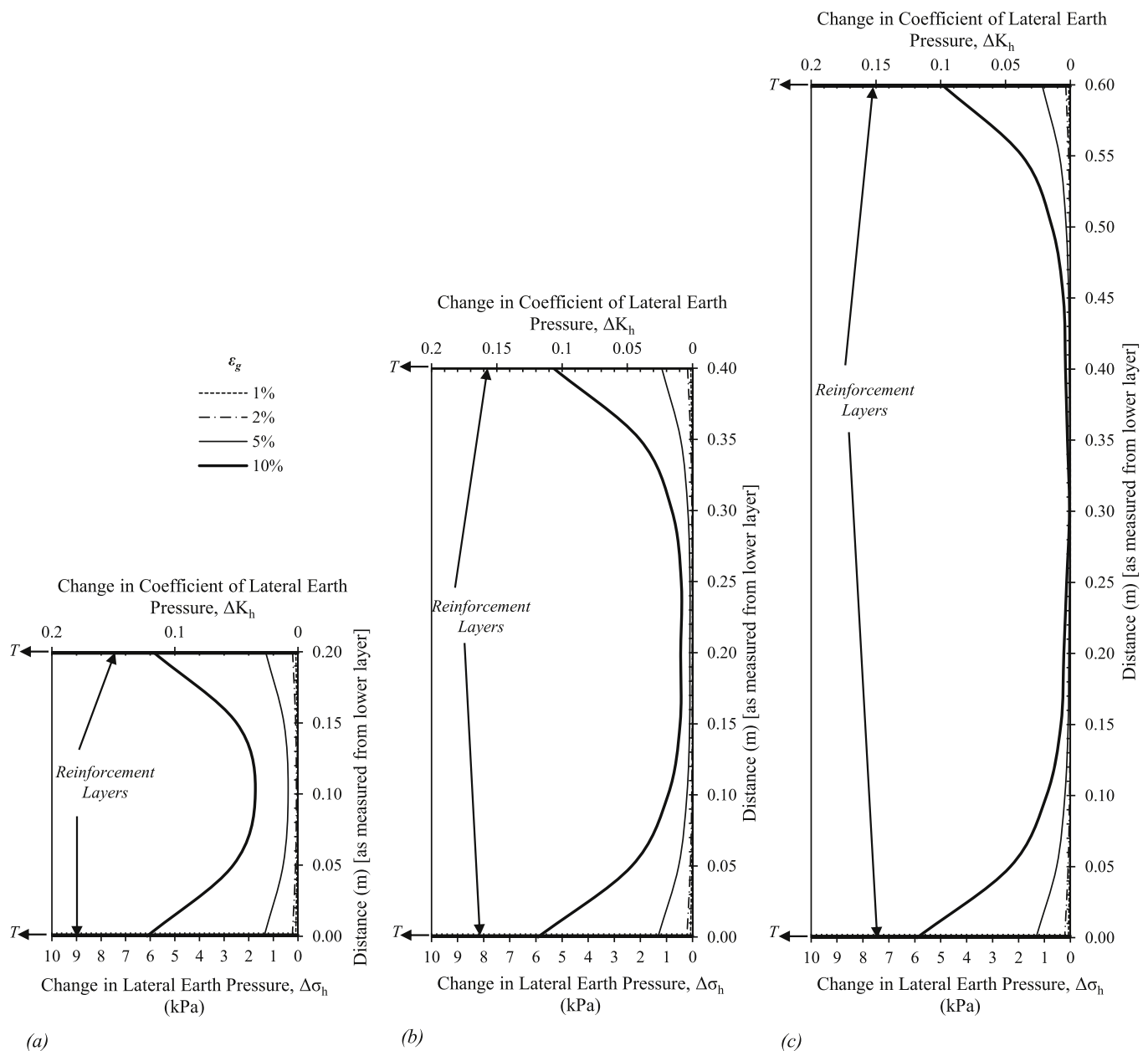
Fig. 19. Change in lateral earth pressure profile for an individual soil layer at various tensile strains in bordering reinforcements: (a) 0.2-m reinforcement vertical spacing; (b) 0.4-m reinforcement vertical spacing; and (c) 0.6-m reinforcement vertical spacing.

reinforcement tensile strains (0, 1, 2 and 5%), which correspond to working stresses in reinforced soil structures. As the figure demonstrates, the change in lateral earth pressure is more uniform in the soil layer with closely-spaced reinforcements (Fig. 19a) than in the soil layer with widely-spaced reinforcements (Fig. 19c).

In short, to solve for the change in the lateral earth pressure, shear stresses generated in the soil due to soil-reinforcement interaction should be estimated. A number of empirical parameters where introduced and developed in this study that can be summarized as follows: (1) the parameters *c* and *b* are fitting parameters to the shape of the reinforcement displacement profile and can be determined by a standard pullout test specified in ASTM D6706 (2013) commonly used to assess the soil-reinforcement interaction. Alternatively, the parameters *c* and *b* can be obtained using Eqn. (7) and (8), respectively, as presented in this study using readily available design parameters. These parameters are needed to predict the soil displacement adjacent to an active reinforcement layer, $\delta_{s,max}$; (2) the critical normal distance, y_{cr}, which

represents the zone of influence of active reinforcement on the state of stresses of the soil in vicinity and was identified by Morsy et al. (2019a) to be 0.3 m; (3) the parameter *f* is a fitting parameter to the curvature of the soil displacement profile, which can be assumed 2.2 in absence of experimental data, as discussed in this study.

6. Implications for design of reinforced soil systems

The relationships developed in this study projects some implications for the design philosophy of several reinforced soil systems. Prior to this study the lateral stress state could not be determined. This is because the lateral stress state is not constant in a horizontal plane along a reinforcement layer and changes during loading (Chandrasekaran et al. 1989; Elton and Patawaran, 2004). As a reinforced soil mass is loaded, the lateral stresses within the reinforced soil mass decrease, but are not uniform across the mass (Elton and Patawaran, 2004). Reinforced soil structures with relatively inextensible reinforcements tend to exhibit

higher lateral earth pressure magnitudes than this with relatively extensible reinforcements, especially at low vertical stress values (Mitchell and Villet, 1987). This study shows that the lateral earth pressure changes with changing the strain in reinforcements. During construction, soil layers are placed in an at-rest condition (or higher if compaction induced stresses are significant) and the corresponding reinforcement layer is placed non-tensioned. With the construction of subsequent layers, reinforcements layers begin to mobilize tensile strength and strain laterally as the adjacent soil layers strain laterally and the lateral earth pressure decreases. For instance, Chandrasekaran et al. (1989) reported that as the geosynthetic friction is mobilized, the soil changes state from at-rest condition to active condition. Also, Elton and Patawaran (2004) reported that a lateral earth pressure coefficient of K_o–K_a was found to provide good agreement between the predicted and measured behavior of large-scale cylindrical reinforced soil masses tested to failure under in an unconfined compression setup.

Reinforcement tensile stresses in a reinforced soil wall are usually calculated based on the lateral earth pressure of tributary areas around each reinforcement layer (usually the reinforcement vertical spacing, S_v). This lateral earth pressure is commonly calculated using a coefficient of lateral earth pressure that ranges from K_a to 2.5 K_a, where K_a is the Rankine coefficient of active lateral earth pressure, depending on the stiffness of the reinforcing elements (*e.g.*, Christopher, 1993), where the coefficient of lateral earth pressure for walls reinforced with geosynthetics is K_a, as a conservative value.

As discussed earlier, this study shows that the change in lateral earth pressure increases with increasing reinforcement strain. Fig. 20 presents the change in coefficient of lateral earth pressure, ΔK_h, averaged over reinforcement spacing, S_v, with reinforcement tensile strain, ε_g, vertical earth pressure, σ_v, and reinforcement vertical spacing, S_v. For the same change in lateral earth pressure the reinforcement strain in reinforced soil walls with comparatively smaller vertical spacings is lower than those in walls with comparatively large vertical spacings. While the change in lateral earth pressure is small at large stresses, it should be noted that the layers exposed to large stresses have been exposed to strain at small stresses prior to their exposure to the higher stresses during construction. Thus, the decrease in lateral stress has already occurred during construction.
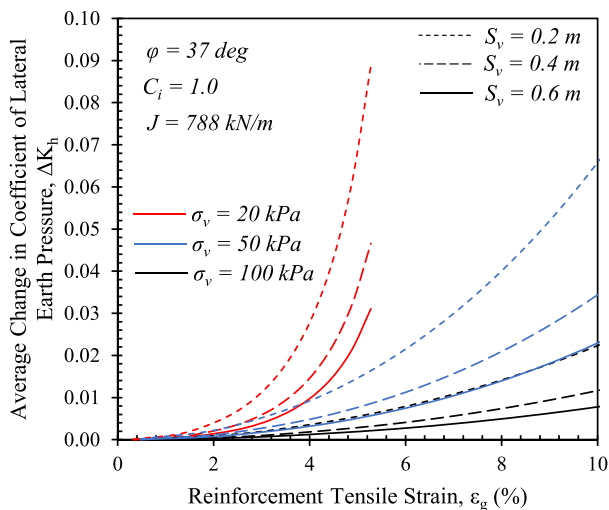

Fig. 20. Average change in coefficient of lateral earth pressure with reinforcement tensile strain, ε_g, vertical earth pressure, σ_v, and reinforcement vertical spacing, S_v.

7. Conclusions

This paper presents analytical solutions to the reinforced soil stress and strain regimes caused by soil-reinforcement interaction. The analytical solutions were developed considering classical theories of continuum mechanics, as well as measurements and observations from soil-reinforcement interaction tests. Analytical models were developed to describe the evolution of displacements and strains in the reinforcement, soil-reinforcement interface, and soil mass. These models were calibrated using experimental data with a wide range of testing parameters. Additionally, models were developed to describe the evolution of the various stresses generated in the reinforcement, soil-reinforcement interface, and soil mass as tensile loading is applied to a reinforcement layer. Subsequently, the concept of the superposition of stresses resulting from individual reinforcement layers was adopted to develop analytical solutions for stresses developing among a group of reinforcement layers considering varying reinforcement vertical spacings. Consequently, the stresses in a reinforced soil system were estimated using the soil stresses estimated for an individual reinforced soil unit. This investigation yielded the following findings:

- The tensile load distribution on an actively loaded reinforcement could be defined by two constants: the curvature of the reinforcement displacement profile and the curvature of the relationship between the front and end reinforcement displacements. These constants could be developed experimentally as functions in the vertical normal stress, σ_v, the reinforcement tensile stiffness, J, and the coefficient of soil-reinforcement interaction, C_i.

- The ability of the reinforcement to transfer load to the soil as well as its neighboring reinforcement layers increases with increasing the interaction between the reinforcement and soil. This ability was represented in this study by measuring the ratio of the soil displacement adjacent to the reinforcement and the reinforcement displacement. This ratio was found to be practically constant under working load conditions (*i.e.*, the relationship between the horizontal soil displacements adjacent to the reinforcement and the reinforcement displacements is linear). The soil to reinforcement displacement ratio was found to increase with increasing the normal stress, σ_v, and the soil-reinforcement interaction coefficient, C_i; whereas, it was found to decrease with increasing the reinforcement vertical spacing, S_v.

- The presented analyses could predict the horizontal stress distribution within the soil adjacent to the reinforcement layer. The change in the horizontal stress increased with increasing the tensile load in the reinforcement and decreased with distance normal to the reinforcement.

- By superposition, the model was used to estimate the change in the horizontal stress within a soil layer between two actively loaded reinforcement layers. The percent change in the horizontal stresses was found to increase with decreasing reinforcement vertical spacing where the entire thickness of the soil layer is affected by the presence of the reinforcement inclusions. That is, as the reinforcement spacing decreases, the interaction among reinforcement layers increases. Overall, it was concluded that the change in the lateral earth pressure increases with increasing reinforcement tensile strain and reinforcement vertical spacing, and it decreases with increasing vertical stress.

- The study presented new insights into the soil-reinforcement interaction loading and straining mechanisms. A reinforced soil wall was used as an example of reinforced soil applications to illustrate how the analyses conducted in this study and the developed models can be of use in practice. The lateral earth pressures in reinforced soil walls develop primarily during construction where the layers strain laterally as construction advances and subsequent layers are constructed. Concurrently, reinforcement layers strain axially and

mobilize tensile strength as the lateral earth pressure within the soil mass decreases.

Notations

First. Greek-letter symbols in alphabetical order [dimensions are in square brackets]

γ_s	Soil shear strain [-]
δ_s	Horizontal soil displacement [L]
$\delta_{s,max}$	Maximum horizontal soil displacement [L]
δ_{sg}	Geosynthetic displacement relative to soil [L]
ε_g	Geosynthetic tensile strain [-]
θ	Angle of principal stress rotation [-]
σ_1	Major principal stress [ML^{-1}T^{-2}]
σ_3	Minor principal stress [ML^{-1}T^{-2}]
σ_h	Horizontal earth pressure [ML^{-1}T^{-2}]
σ_v	Vertical earth pressure [ML^{-1}T^{-2}]
τ_s	Shear stress in soil [ML^{-1}T^{-2}]
τ_{sg}	Soil-geosynthetic interface shear stress [ML^{-1}T^{-2}]
ϕ	Angle of soil internal friction [-]
ϕ_{sg}	Angle of soil-geosynthetic interface friction [-]

Second. Roman-letter symbols in alphabetical order [dimensions are in square brackets]

A	Parameter for the geosynthetic displacement function corresponding to the end displacement asymptote [L]
B	Parameter for the geosynthetic displacement function corresponding to the difference between the front displacement and end displacement asymptote [L]
b	Curvature parameter of the relationship between the front and end displacements of a displacing reinforcement [-]
C_c	Curvature coefficient [-]
C_i	Soil-reinforcement interaction coefficient [-]
C_u	Uniformity coefficient [-]
c	Parameter for the geosynthetic displacement function representing a curvature parameter [-]
D	Particle size [L]
D_{50}	Mean particle size [L]
e_{max}	maximum void ratio [-]
e_{min}	minimum void ratio [-]
F	Soil to reinforcement displacements ratio dependency factor on the distanced from the loading front [-]
f	Curvature parameter of the soil displacement profile normal to soil-reinforcement interface [-]
G	Soil shear modulus [ML^{-1}T^{-2}]
G_s	Specific gravity [-]
J	Reinforcement tensile stiffness [MT^{-2}]
K_a	Coefficient of Rankine's active lateral earth pressure [-]
K_h	Coefficient of active lateral earth pressure in the soil-reinforcement influence zone [-]
L	Reinforcement embedment length [L]
m	Reinforcement vertical spacing exponent [-]
N	Ratio of major to minor principal stresses [-]
n	Stress exponent [-]
p_o	atmospheric pressure (1 atm) [ML^{-1}T^{-2}]
q	Surcharge stress [ML^{-1}T^{-2}]
S_v	Reinforcement vertical spacing [L]
$S_{v,cr}$	Critical reinforcement vertical spacing [L]
$S_{v,ref}$	Reference reinforcement vertical spacing [L]
T_g	Reinforcement tensile force per unit length [MT^{-2}]
T_{ult}	Reinforcement ultimate tensile strength [MT^{-2}]
$T_{@5\%}$	Reinforcement tensile strength at 5% axial strain [MT^{-2}]
$u1$ *through* $u10$	Points where displacements $u_{g,u1}$ *through* $u_{g,u10}$, respectively, are measured in the active reinforcement [-]
u_g	Displacement in the active reinforcement at horizontal

	distance from the loading front, x [L]
$u_{g,u1}$ *through* $u_{g,u10}$	Displacements measured at points $u1$ to $u10$ in the active reinforcement [L]
$v1$ *through* $v5$	Points where displacements $v_{g,v1}$ *through* $v_{g,v5}$, respectively, are measured in the upper passive reinforcement [-]
v_g	Displacement in the upper passive reinforcement [L]
$v_{g,v1}$ *through* $v_{g,v5}$	Displacements measured at points $v1$ to $v5$ in the upper passive reinforcement [L]
$w1$ *through* $w5$	Points where displacements $w_{g,w1}$ *through* $w_{g,w5}$, respectively, are measured in the lower passive reinforcement [-]
w_g	Displacement in the lower passive reinforcement [L]
$w_{g,w1}$ *through* $w_{g,w5}$	Displacements measured at points $w1$ to $w5$ in the lower passive reinforcement [L]
x	Horizontal distance from the loading front [L]
y	Vertical distance from the soil-geosynthetic interface [L]
y_1 and y_2	Vertical distances from two soil-geosynthetic interfaces bordering a soil layer [L]
y_{cr}	Critical vertical distance from the soil-geosynthetic interface [L]

References

Abramento, M., Whittle, A.J., 1995. Analysis of pullout tests for planar reinforcements in soil. J. Geotech. Eng. 121 (6), 476–485.

Adams, M., Nicks, J., Stabile, T., Wu, J.T., Schlatter, W., Hartmann, J., 2011. Geosynthetic Reinforced Soil Integrated Bridge System, Synthesis Report. Report No. FHWA-HRT-11-027. Federal Highway Administration, McLean, Virginia, United States.

Alagiyawanna, A.M.N., Sugimoto, M., Sato, S., Toyota, H., 2001. Influence of longitudinal and transverse members on geogrid pullout behavior during deformation. Geotext. Geomembranes 19 (8), 483–507.

ASTM D4595-17, 2017. Standard Test Method for Tensile Properties of Geotextiles by the Wide-Width Strip Method. ASTM International.

ASTM D6706-01, 2013. Standard Test Method for Measuring Geosynthetic Pullout Resistance in Soil. ASTM International.

Chandrasekaran, B., Broms, B., Wong, K.S., 1989. Strength of fabric reinforced sand under axisymmetric loading. Geotext. Geomembranes 8, 293–310.

Djeffal, H., Belkacemi, S., 2020. Effect of soil-reinforcement interaction coefficient on reinforcement tension distribution of reinforced slopes. Geotext. Geomembranes 48 (4), 572–580.

Ebrahimian, B., Noorzad, A., Alsaleh, M.I., 2012. "Modeling shear localization along granular soil–structure interfaces using elasto-plastic Cosserat continuum. Int. J. Solid Struct. 49 (2), 257–278.

Edil, T.B., Bosscher, P.J., Sundberg, A.J., 2006. Soil-structure interface shear transfer behavior. In: In Geomechanics II: Testing, Modeling, and Simulation, pp. 528–543.

Elton, D.J., Patawaran, M.A.B., 2004. Mechanically stabilized earth reinforcement tensile strength from tests of geotextile-reinforced soil. In: *Transportation Research Record: Journal of the Transportation Research Board*, 1868, TRB. National Research Council, Washington, D.C., pp. 81–88.

Holtz, R.D., Lee, W.F., 2002. Internal Stability Analyses of Geosynthetic Reinforced Retaining Walls. Report No. WA-RD 532.1. Washington State Department of Transportation, Olympia, Washington.

Hu, L., Pu, J., 2004. Testing and modeling of soil-structure interface. J. Geotech. Geoenviron. Eng. 130 (8), 851–860.

Juran, I., Guermazi, A., Chen, C.L., Ider, M.H., 1988. Modelling and simulation of load transfer in reinforced soil: Part 1. Int. J. Numer. Anal. Methods GeoMech. 12 (2), 141–155.

Kharchafi, M., Dysli, M., 1993. Study of soil-geotextile interaction by an X-ray method. Geotext. Geomembranes 12 (4), 307–325.

Lashkari, A., Jamali, V., 2020. Global and local sand–geosynthetic interface behaviour. Geotechnique. https://doi.org/10.1680/jgeot.19.P.109.

Leshchinsky, D., Kaliakin, V., Bose, P., Collin, J., 1994. "Failure mechanism in geogrid-reinforced segmental walls: experimental implications." *Soils and Foundations. Journal of the Japanese Society of Soil Mechanics and Foundation Engineering* 34 (4), 33–41.

Leshchinsky, D., Vulova, C., 2001. Numerical investigation of the effects of geosynthetic spacing on failure mechanisms in MSE block walls. Geosynth. Int. 8 (4), 343–365.

Mitchell, J.K., Soga, K., 2005. Fundamentals of Soil Behavior. John Wiley & Sons, Hoboken, NJ.

Morsy, A.M., 2017. Evaluation of Soil-Reinforcement Composite Interaction in Geosynthetic-Reinforced Soil Structures. Ph.D. Dissertation. The University of Texas at Austin, Austin, Texas, USA, p. 635p.

Morsy, A.M., Leshchinsky, D., Zornberg, J.G., 2017a. Effect of reinforcement spacing on the behavior of geosynthetic-reinforced soil. In: In Proceedings of Geotechnical Frontiers 2017, American Society of Civil Engineers (ASCE), March 12-15, 2017 | Orlando, Florida, USA, pp. 112–125.

Morsy, A.M., Zornberg, J.G., Christopher, B.R., Leshchinsky, D., Tanyu, B.F., Han, J., 2017b. Experimental approach to characterize soil-reinforcement composite interaction,. In: *Proceedings of the 19th International Conference on Soil Mechanics and Geotechnical Engineering (19th ICSMGE)*, International Society for Soil Mechanics and Geotechnical Engineering (ISSMGE), September 17-22, 2017 | Seoul, Korea, pp. 451–454.

Morsy, A.M., Roodi, G.H., Zornberg, J.G., 2018. "Evaluation of soil-reinforcement interface shear band. In: *In Proceedings of the 11th International Conference on Geosynthetics (11th ICG): Properties and Testing – Reinforcement*, International Geosynthetics Society (IGS), September 16-21, 2018 | Seoul, Korea, Paper No. S18-05.

Morsy, A.M., Zornberg, J.G., Leshchinsky, D., Han, J., 2019a. Soil-reinforcement interaction: effect of normal stress and reinforcement spacing. J. Geotech. Geoenviron. Eng. 145 (12). December 2019, 04019115.

Morsy, A.M., Zornberg, J.G., Han, J., Leshchinsky, D., 2019b. A new generation of soil-geosynthetic interaction experimentation. Geotext. Geomembranes 47 (3), 352–368.

Morsy, A.M., Zornberg, J.G., Leshchinsky, D., Christopher, B.R., Han, J., Tanyu, B.F., 2020. Experimental evaluation of the interaction among neighboring reinforcements in geosynthetic-reinforced soils. J. Geotech. Geoenviron. Eng. 146 (10) https://doi.org/10.1061/(ASCE)GT.1943-5606.0002365.

Nicks, J.E., Adams, M.T., Ooi, P.S.K., Stabile, T., 2013. Geosynthetic Reinforced Soil Performance Testing—Axial Load Deformation Relationships. Report No. FHWA-HRT-13-066.

Ochiai, H., Otani, J., Hayashic, S., Hirai, T., 1996. The pull-out resistance of geogrids in reinforced soil. Geotext. Geomembranes 14 (1), 19–42.

Palmeira, E.M., 2009. Soil-geosynthetic interaction: modelling and analysis. Geotext. Geomembranes 27 (5), 368–390.

Peng, X., Zornberg, J.G., 2019. Evaluation of soil-geogrid interaction using transparent soil with laser illumination. Geosynth. Int. 26 (2), 206–221.

Roodi, G.H., Morsy, A.M., Zornberg, J.G., 2018. "Soil–geosynthetic interface shear in different testing scales. Transport. Res. Rec. 2672 (52), 129–141.

Rotta Loria, A.F., Laloui, L., 2016. The interaction factor method for energy pile groups. Comput. Geotech. 80, 121–137.

Wang, Z., Jacobs, F., Ziegler, M., 2016. "Experimental and DEM investigation of geogrid–soil interaction under pullout loads. Geotext. Geomembranes 44 (3), 230–246.

Werner, G., Resl, S., 1986. Stability mechanisms in geotextile reinforced earth-structures. In: *In Proceedings of 3rd International Conference on Geotextiles: Slope Protection and Retaining Walls*, Vienna, Austria, pp. 1131–1135.

Wu, J.T., Pham, T.Q., Adams, M.T., 2013. Composite Behavior of Geosynthetic Reinforced Soil Mass. Report No. FHWA-HRT-10-077. Federal Highway Administration, McLean, Virginia, United States.

Wu, J.T.H., 2019. Characteristics of geosynthetic reinforced soil (GRS) walls: an overview of field-scale experiments and analytical studies. Transp. Infrastruct. Geotech. 6, 138–163.

Xu, C., Liang, C., Shen, P., 2019. Experimental and theoretical studies on the ultimate bearing capacity of geogrid-reinforced sand. Geotext. Geomembranes 47 (3), 471-428.

Xu, C., Liang, C., Shen, P., Chai, F., 2020. Experimental and numerical studies on the reinforcing mechanisms of geosynthetic-reinforced granular soil under a plane strain condition. Soils Found. 60 (2), 466–477.

Zornberg, J.G., Roodi, G.H., Gupta, R., 2017. "Stiffness of soil–geosynthetic composite under small displacements: i. model development. J. Geotech. Geoenviron. Eng. 143 (10), 04017075.

Zornberg, J.G., Morsy, A.M., Mofarraj, B., Christopher, B.R., Leshchinsky, D., Han, J., Tanyu, B.F., Gebremariam, F.T., Shen, P., Jiang, Y., 2018. Defining the Boundary Conditions for Composite Behavior of Geosynthetic Reinforced Soil (GRS) Structures. National Cooperative Highway Research Program (NCHRP), Project 24-41. Transportation Research Board, Washington DC, October, p. 986p.

Zornberg, J.G., Morsy, A.M., Mofarraj, B., Christopher, B.R., Leshchinsky, D., Han, J., Tanyu, B.F., Gebremariam, F.T., Shen, P., Jiang, Y., 2019. Proposed Refinements to Design Procedures for Geosynthetic Reinforced Soil (GRS) Structures in AASHTO LRFD Bridge Design Specifications. National Cooperative Highway Research Program (NCHRP), Project 24-41. Transportation Research Board, Washington DC, p. 64p. March.